An MRI Actuated and Imaged Concentric Tube Catheter

Peter Lloyd
p.lloyd@leeds.ac.uk

University of Leeds https://orcid.org/0000-0002-4927-071X
Nikita Murasovs
University of Leeds
Yael May
University of Leeds https://orcid.org/0009-0002-4143-7201
Alistair Bacchetti
University of Leeds
Ben Calme
University of Leeds
joshua Davy
University of Leeds
Vittorio Francescon
University of Leeds
James Chandler
University of Leeds https://orcid.org/0000-0001-9232-4966
Erica Dall'Armellina
University of Leeds https://orcid.org/0000-0002-2165-7154
Jurgen Schneider
University of Leeds
Pietro Valdastri
University of Leeds https://orcid.org/0000-0002-2280-5438

Article

Keywords:

Posted Date: November 7th, 2025

DOI: https://doi.org/10.21203/rs.3.rs-7629088/v1

Additional Declarations: There is **NO** Competing Interest.

An MRI Actuated and Imaged Concentric Tube Catheter

Peter Lloyd [*][†] **and Nikita Murasovs**[†], Yael L. May, Alistair Bacchetti,
Benjamin Calmé, Joshua Davy, Vittorio Francescon, James H. Chandler,
Erica Dall'Armellina, Jurgen E. Schneider, Pietro Valdastri[*]

Abstract

Two major challenges associated with robotic catheterization are, (a) the provision of controllable degrees of freedom (DoFs) and, (b) accessing feedback on the shape and pose of the catheter, safely and at a useful diameter-scale. Miniaturizable active steering can be provided via magnetic actuation and MRI offers high definition, radiation free, 3D images which can be leveraged as a shape sensor. For the higher controllable DoFs required for shape forming these two solutions are currently incompatible. Here, we propose a structurally adaptable "Coaxial Sleeve Magnetic Actuator" (CoSMA), driven by the background field of the MRI scanner. This enables multi-DoF motion and real-time feedback, both via the MRI system. Our approach combines the magnetic actuation principle of the easy axis of alignment with the mechanical principles of concentric tube designs. This concept allows for a materially flexible ($E = \mathcal{O}(1\,\mathrm{MPa})$), and therefore risk reduced, multi-DoF catheter. Low magnetic volume required for actuation minimizes imaging artifacts caused by magnetic elements permitting a view of both the CoSMA and the surrounding anatomy. We demonstrate the CoSMA, constructed of three coaxial components, two sleeves and one guidewire, with respective outer diameters of 3 mm, 1.5 mm and 0.4 mm, in an aortic arch phantom navigation within the bore of a pre-clinical MRI scanner.

1 Introduction

Soft active catheters have demonstrated their efficacy in accessing sensitive, restricted, and unstructured regions of the human anatomy [1] [2]. Magnetically actuated devices have proven of particular interest due to a combination of material softness and extensive miniaturization potential [3]. Flexible Magnetic Catheters (FMCs) can provide a safer and more controllable pathway to otherwise inaccessible regions of the body offering clinical solutions not otherwise available [4]. In parallel to this, concentric tube robots (also known as active cannulas), offer high Degree of Freedom (DoF) deformation along an elastic continuum structure which can be fabricated at the millimetre scale [5] and have been shown to be MRI compatible [6]. Concentric tube robots are made from several pre-curved tubes nested within one another and rely on material elasticity to transfer deformation energy from the operator to the robot. As such, they are typically made from Nitinol (Elastic modulus, E $\approx$ 50 GPa) which is stiff in comparison to living tissue. Furthermore, due to this inherent stiffness, these robots also suffer from the "snap-through instability", where the robot can physically snap from one low energy configuration to another [7, 8]. Concentric tube robots leveraging magnetic actuation to enhance stability [9] or reduce stiffness [10] [11] have been demonstrated but never in an MRI compatible format. Here, we offer a fully hybridized approach combining the mechanical

---

[*] Corresponding authors: p.lloyd@leeds.ac.uk and p.valdastri@leeds.ac.uk

[†] Peter Lloyd and Nikita Murasovs are the joint first authors of this work.

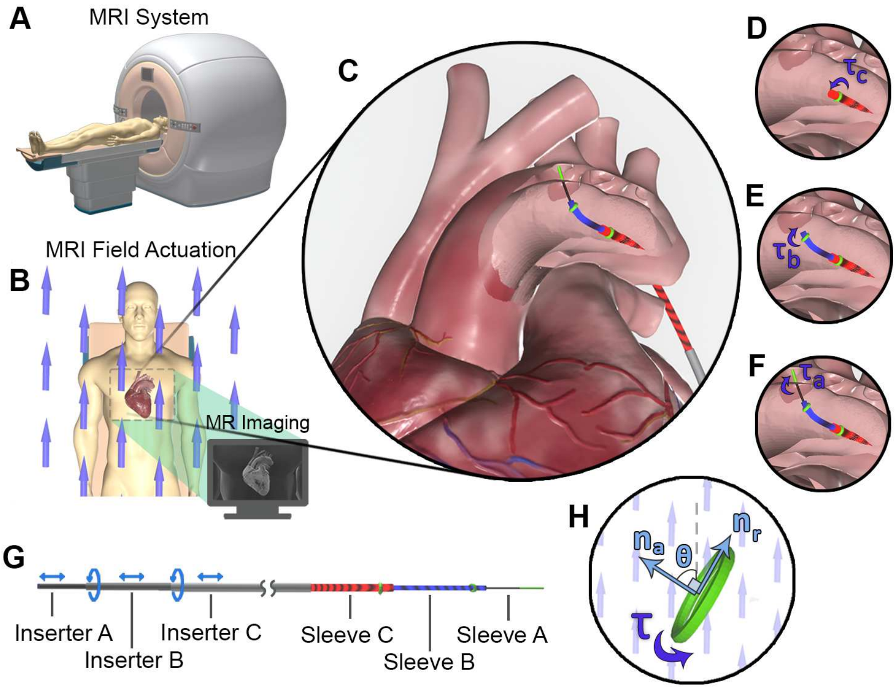

Figure 1: The operating principle of our Coaxial Sleeve Magnetic Actuator (CoSMA). All MRI systems provide a very strong, static homogeneous background field - B_0 (A,B). Softly ferromagnetic rings align their path of lowest demagnetization (n_r) with B_0 (H). These rings are connected to a series of coaxial sleeves (C,D,E,F), translation and orientation of which is controlled by the operator (G) - these base configurations map to deformations of the CoSMA (See Supplementary Video S1). The entire system can be monitored in high definition 3D via MR Imaging.

principles of concentric tube designs with the off-board energy provision of magnetic actuation to create a softer, and therefore safer, design, MRI compatible by design, and with less susceptibility to the snap-through instability.

One of the major outstanding issues associated with the navigation of FMCs relates to device tracking, typically performed via fluoroscopy, which exposes both patient and operators to ionising radiation whilst providing a low contrast 2D projection. Alternative sensing solutions to fluoroscopy do exist and have demonstrated encouraging results (at significantly lower cost than MRI) but are variously limited in terms of fidelity (e.g. ultrasound [12]), material stiffness (e.g. Fibre Bragg Gratings [13]) or, in the case of electromagnetic tracking (e.g. [14]), provide singular pose feedback per sensor, imposing limits on both information availability and minimum physical size. Magnetic Resonance Imaging (MRI) offers the current gold standard in non-ionizing high-resolution 3D imaging and thus, "MRI-compatible robotics" (primarily, robots made of MRI-safe, non-ferrous materials) represents an active area of research with high potential [15].

MRI actuated robotics represents an alternative paradigm to the aforementioned approaches where a robot is actuated *and* imaged by the MRI system [16]. This methodology has the potential to enable MRI-guided procedures where diagnosis, surgery, and post-treatment assessment can all be performed in a single, integrated event. Research has been conducted in this field utilizing the imaging gradients (e.g. [17–21]), the fringe field [22] and the interaction between a controllable current through embedded micro-solenoids and the background field [23, 24]. The challenges associated with the approaches used to date are the low magnitude and limited DoFs of force available via gradient coil actuation, the difficulties of miniaturization of embedded solenoids and the lack of imaging when utilising the fringe field for actuation. Here we introduce our Coaxial Sleeve Magnetic Actuator (CoSMA) which leverages the phenomenon of the *easy axis of alignment* coupled with mechanical control of position and orientation of coaxial sleeves (Fig. 1). This design offers a solution for a soft, miniaturizable, shape-forming catheter which can be sensed, and therefore controlled, via the MR system.

2 Principle of Operation

Any magnetically actuated soft robot operates via balancing internal elastic energy with an externally applied magnetic field. Primarily, traditional magnetic soft robots have relied on a hard magnetic remanence stored within the robot's structure, actuated by relatively low externally applied fields [25]. Within the bore of any MRI system, we have an ultra-high, mono-axial background field ($B_0 \in (1, 7)T$) and a much smaller tri-axial gradient ($\nabla B_0 \in (0, 600)mT/m$) available for actuation purposes (the magnitude of the radio-frequency fields are too small to impact actuation). The background field is sufficiently strong that no magnetic remanence can be retained. Thus, the concept of "magnetically hard materials" whereby materials hold a permanent vector of magnetization becomes redundant and, consequently, well-explored modes of magnetic manipulation become obsolete [26].

A non-spherical magnetic object exposed to a background field will experience a torque attempting to align the longest (principle) axis with the background field [27, 28]. This easy axis alignment is traditionally considered to be too weak for robotic applications above the micro-scale but a sufficiently large field (such as the B_0 field of a clinical MRI system) can be leveraged to generate considerable deformation. Our design takes advantage of the large magneto-static energy available via the B_0 field and moves the actuation of controllable DoFs outside of the system. Magnetic energy is provided by the background field, and ferrous rings embedded at the tip of each sleeve translate this energy into deformation. By rotating and translating the sleeves we can create a variety of shapes which ultimately enable tortuous navigation (Fig. 1). The choice of rings as the magnetically active component (as opposed to ellipsoids or rods) derives from their natural conformity to the cylindrical shape of the CoSMA. Slender, linear rods mounted at various angles along the length of the catheter are easier to model (see Section 5.3) but inherently length-limited and thus torque-limited. These rings are agnostic to imaging gradients and can thus be simultaneously imaged. The design principle is conceptually similar to that of the concentric tube designs in [29, 30] (which also rely on rotating and translating cores) but, as deformation energy is provided magnetically rather than via elastic restoration, the material construction of the CoSMA can be of the order of three orders of magnitude softer. This relative softness can improve patient safety but, less intuitively, when combined with the material anisotropy of the braided design (See Section 5.2) also mitigates the snap-through instability commonly observed in concentric tube designs [5].

Magnetic torque due to easy-axis alignment can be shown to be a function of geometry - demagnetization factors (n_r, n_a) and volume (v), saturation magnetization of the material (m_s), and θ, the angle between B_0 and the global frame direction of n_a [31] (Fig. 1G, see Section 5.3 for a detailed explanation),

$$\tau_{mag} = \frac{1}{2}\mu_0 v|n_r - n_a|m_s^2 sin(2\theta), \tag{1}$$

where μ_0 is the vacuum permeability.

Due to the presence of $sin(2\theta)$ in Equation 1 it is evident that *no deformation greater than 90° is possible with a single magnetic entity.* An intuitive result as the induced polarity of a soft magnet is free to flip giving a maximum range of motion of 180° as opposed to the 360° provided with magnetically hard designs [32]. This is a key point which has motivated this work - in order to allow deformations greater than 90° we have combined multiple coaxial sleeves with different referential configurations.

A near-orthogonally mounted ring (e.g. referential angle, $\theta_0 = 85°$, see Fig. 2) will, depending on magnetic energy and elastic stiffness, asymptotically converge on an 85° deformation. This curvature can be regulated in the design phase via magnetic geometry and in the actuation phase via stiffness modulation (more on this in Section 3.1). Thus, our outer sleeve (henceforth referred to as sleeve C), manufactured from 3 mm diameter nylon braid (see Section 5.6) and with a 4 mm diameter iron ring affixed to the tip, can provide deformation up to, but never exceeding, $\theta_{C0} = 85°$ (in the numerical formulation (Section 5.5) these angles and torques are three-dimensional but for the purposes of this conceptual explanation we adopt planar notation).

A second sleeve (sleeve B), manufactured from 1.5 mm diameter nylon braid, is free to translate and rotate within sleeve C but constrained to follow the same curvature up to the distal point of sleeve C. Were sleeve B to host a ring with the same referential angle as sleeve C it would be subject to the same constraints and thus, deformation beyond 90° (retroflexion) would not be possible. The referential ring orientation on sleeve B (θ_{B0}) is one of the key variables considered in the numerical formulation (Section 5.5). Clearly, the magnitude of the magnetic torque relative to that on sleeve C is critical but, assuming a correctly balanced system, retroflexion can be achieved via manipulation of θ_{B0}. Letting $\theta_{B0} = 45°$, sleeve B will either align in the forward facing, lowest elastic energy, configuration (Fig. 2C) or, via a 180° rotation of sleeve B, will align in the backward facing configuration (Fig. 2F).

A third and final sleeve (sleeve A), manufactured from 0.4 mm nylon wire, carries a straight iron pin which is referentially aligned with B_0, i.e. $\theta_{A0} = 0°$. Clearly, this pin displays different demagnetization factors to the rings leveraged in sleeves B and C, but aside from this, the principle of operation is identical. Sleeve A can be inserted beyond sleeve B or fully retracted out of the system as required. The purpose of this sleeve is simply to extend the range of motion of the CoSMA as demonstrated in Section 3. Importantly, dependent on the configuration of sleeve B, sleeve A will align either forward (Fig. 2A) or backward facing (Fig. 2F).

We use annealed iron wire to fabricate our ferrous components due to high saturation magnetization ($m_s = 1.43 \times 10^6 (A/m)$ [33]). Determination of the demagnetization factors is a non-trivial exercise covered in Section 5.3. Clearly, the angle between external field and symmetrical axis (θ) is a function of both referential pose and catheter deformation and so, in Section 5.5 a simulation is developed which employs a pseudo-rigid link model to balance elastic and magnetic torques throughout the coaxially connected sleeves. We use braided nylon sleeves for our continuum structure as we must be able to transfer torsion whilst allowing bending. The mechanical behaviour of these sleeves is characterized in Section 5.2.

3 Results

3.1 Free Space Demonstration

We show a sample of the range of motion of the CoSMA in free space in Fig. 2. Sleeve C, with a referential ring angle $\theta_{C0} = 85°$ converges upon, but can never exceed 85° of deformation (Fig. 2G). This curvature can be modulated at run-time by inserting a nitinol stiffening rod down the central channel (Fig. 2D). Rotation of sleeve C permits the full 360° range of motion. Sleeve B, with a referential ring angle $\theta_{B0} = 45°$ is shown in the forward facing, lowest elastic energy, configuration (Fig. 2C). The sigmoidal form (Fig. 2B) is achieved after a 180° rotation of sleeve B when sleeve B is *above* the threshold length (see Section 5.5). The backward-facing configuration (Fig. 2F) is

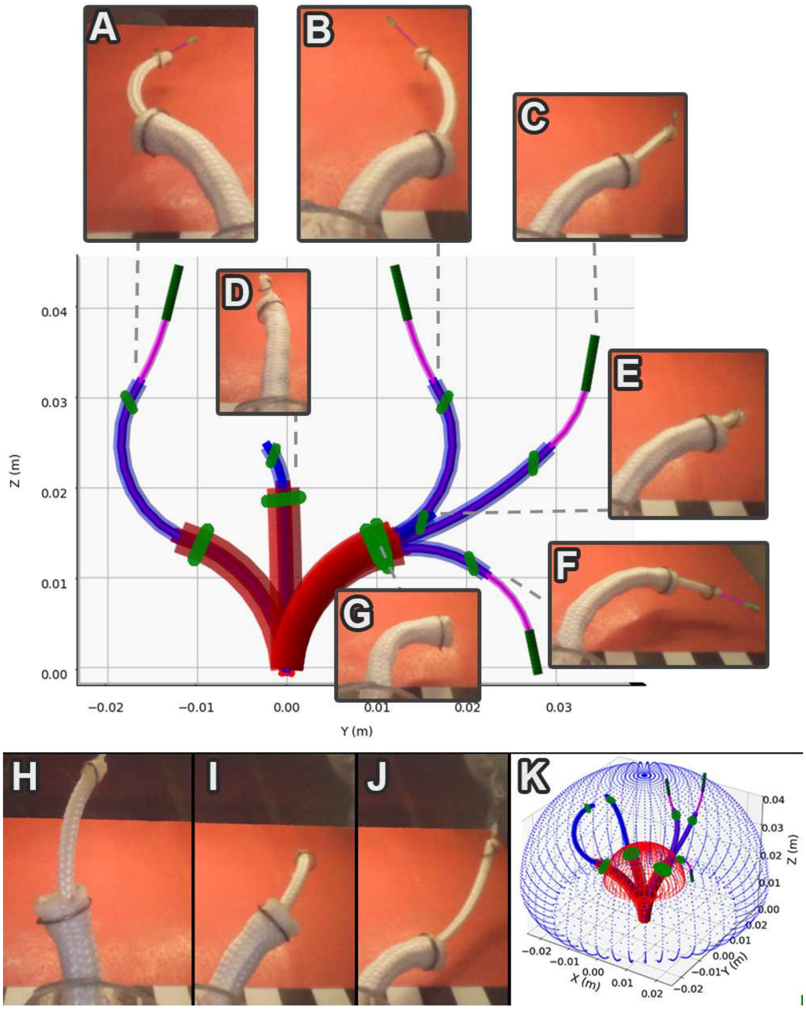

Figure 2: The CoSMA deforming in the bore of the MRI scanner (A-J) (See Supplementary Video S2) and the results of the simulation described in Section 5.5. Sleeve C is shown in red, sleeve B in blue and sleeve A in pink with the magnetically active components shown in green. Sleeve C, with a referential ring angle $\theta_{C0} = 85^\circ$ converges upon, but cannot exceed 85° of deformation as shown in (G). Sleeve B, with a referential ring angle $\theta_{B0} = 45^\circ$ can be easily rotated to alternate between the sigmoidal deformation mode in (A,B) and the forward facing, lowest elastic energy, configuration in (C). Sleeve A will always align with B_0 which, up to this point, is forward. If the 180° rotation of sleeve B is performed below the threshold length of sleeve B as in (E) (see Section 5.5 for details on this transformation) the primary backward-facing configuration is achieved as in (F). At this point sleeve A will align with B_0 in the backward-facing orientation. For required deformations of sleeve C below 85° a nitinol stiffening rod can be inserted shown in (D). (H-J) show three examples of the three-dimensional shapes available by simply rotating sleeves B and C relative to each other and to the global frame. (K) Shows the three-dimensional point cloud of possible sleeve B and C tip positions generated from the simulation in Section 5.5 with four sample catheter shapes.

demonstrated after a 180° rotation of sleeve B when sleeve B is *below* the threshold length (see Section 5.5). All of these deformations are attainable in three dimensions as sampled in Fig. 2H-J.

3.2 Clinical Applicability

To demonstrate the potential for clinical applicability of the CoSMA we navigate the various bifurcations of a 3D printed aortic arch phantom[1]. Navigating the aortic arch is essential in procedures such as angioplasty, endovascular aneurysm repair, and cardiac catheter ablation. Current clinical practice for cardiac catheterization involves the manual insertion of a relatively stiff ($E \approx 200$ MPa [34], see Section 5.2) pre-bent guidewire from the radial (upper limb) or femoral (lower limb) arteries followed by navigation to the aortic arch. The aortic arch gives rise to four main branches: the right and left common carotid arteries and the right and left subclavian arteries. Cardiac catheterization is one of the most common cardiac procedures with more than 1,000,000 performed, either diagnostically or therapeutically, in the United States annually [35]. Intra-procedural complications have been reported with occurrence rates up to 6% and post-procedural complications with occurrence rates up to 33% [36]. Procedural success is reliant, amongst other variables, on the technical skills of the operators [35]. Assisted catheterisation, as well as offering a significant reduction in stiffness, promises to remove this dependency and increase procedural precision [37, 38].

The demonstration in Figs.3-4 and the Supplementary Video S3 illustrates the potential for a trans-femoral approach in which the CoSMA is guided into any branch of the aortic arch, enabling compatibility with the aforementioned procedures, whilst highlighting the CoSMA's dexterity and trackability under MRI guidance. Both Figures are divided into (A) optical camera images, (B) 2D slice of the MR Image (all MRIs were taken in gadolinium doped water (0.5mM Gd-solution)), (C) Reconstruction of anatomy and CoSMA shape based on 3D MRI data (in 3D Slicer software) and (D) 3D rendering of phantom and reconstructed CoSMA shape with signal void centres rendered as grey spheres; camera positions are also shown. The 3D aortic arch prior to CoSMA insertion is shown, then the positions of the CoSMA after navigation into the left subclavian artery (LSA), the left common carotid artery (LCA), the ascending aorta (AA), the right common carotid artery (RCA) and finally, the right subclavian artery (RSA).

All navigations were performed three times using the prototype catheter under visual feedback via manual operation of the base configuration as detailed in Section 5.5.1. The LSA (mean navigation time: 62 ± 24 seconds), LCA (147 ± 81 seconds) and RCA (155 ± 61 seconds) all require forward facing sigmoidal deformations of varying radii of curvature, these being the simplest to navigate. The AA (139 ± 15 seconds) required retroflexion to navigate, and the most demanding route, the RSA (188 ± 45 seconds), required three-dimensional sigmoidal deformation. Nevertheless, a completely inexperienced user managed to navigate to all five targets in under ten minutes. These navigations were performed in air for the purposes of timings and recording the Supplementary Video S3. MR images are distorted by the presence of ferrous bodies in the MRI bore; this distortion, along with imaging time, has been experimentally minimized (Section 5.4). The full navigations were repeated in gadolinium doped water (0.5mM Gd-solution) to obtain the corresponding 3D MR scans (See Section 5.4 for details)) taken at the final pose.

4 Conclusion and Discussion

Our novel catheter design is capable of large multi-DoF deformations which are mechanically controllable from outside the MRI system. Evidently, CoSMA's body is significantly softer than would be possible without harnessing the magneto-static energy of the system. Furthermore, we have used

---

[1] https://www.printables.com/model/661477-aorta

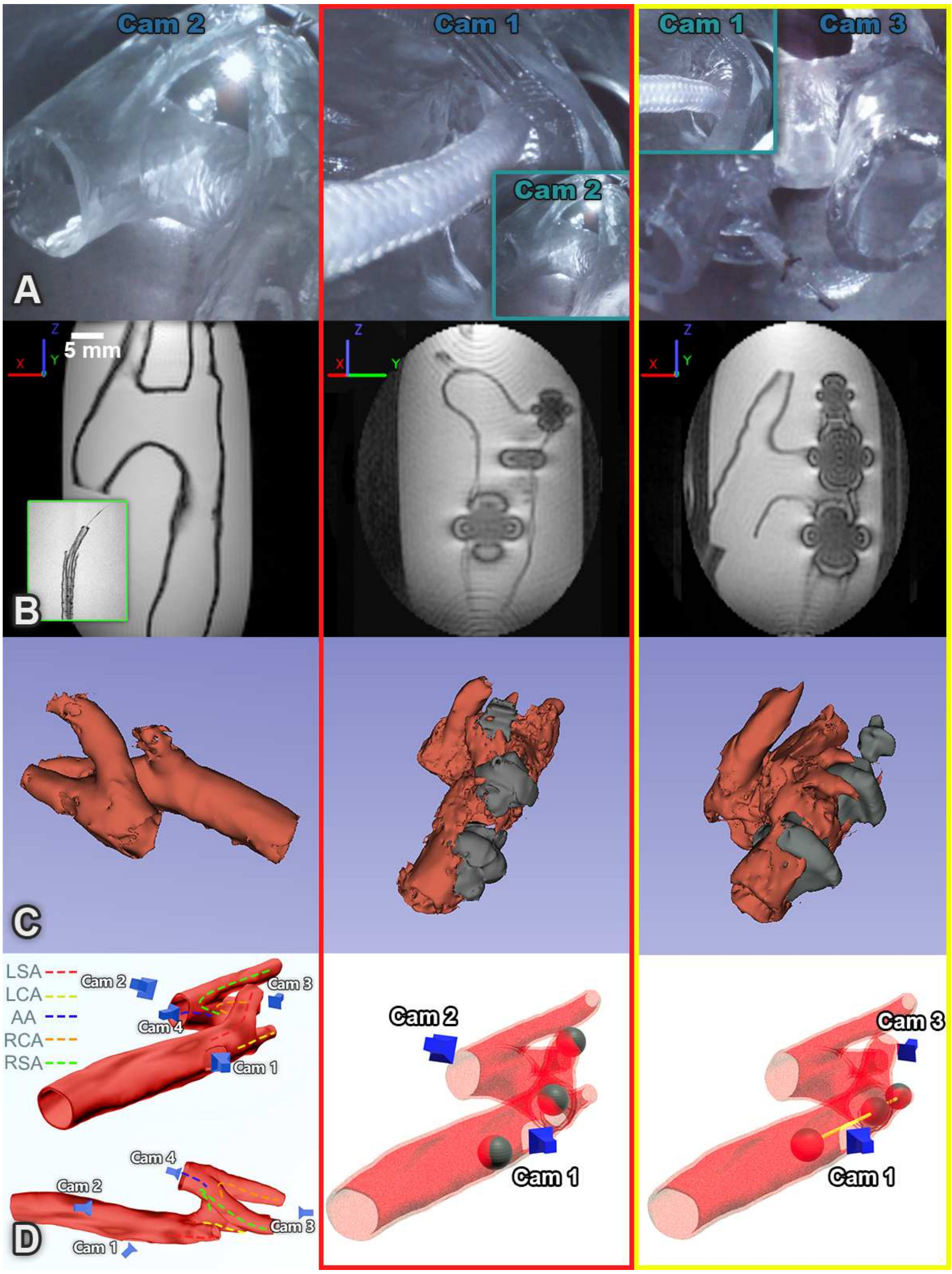

Figure 3: Visual and MR images of the aortic arch navigations. The left-hand column shows the 3D aortic arch prior to CoSMA insertion. The full shape of the phantom can be seen in row C, reconstructed from the 3D MRI. MR images in row B are selected slices so don't show the full geometry. The central column (red surround) shows the CoSMA navigating into the left subclavian artery (LSA). The right-hand column (yellow surround) shows navigation into the left common carotid artery (LCA). (A) Optical camera images. (B) 2D slice of the MR image showing signal voids from ferrous components. Basis frame shown where B_0 always exists in the Z direction. Also shown as insert (green surround) is an MRI of the three-sleeve CoSMA with all metallic components removed. (C) Reconstruction of anatomy and CoSMA shape based on 3D MRI data (3D Slicer 5.8.1 https://www.slicer.org/), and (D) 3D rendering of phantom with reconstructed shape of the CoSMA, signal void positions (shown as grey spheres) and camera positions. All navigations are shown in full in Supplementary Video S3.

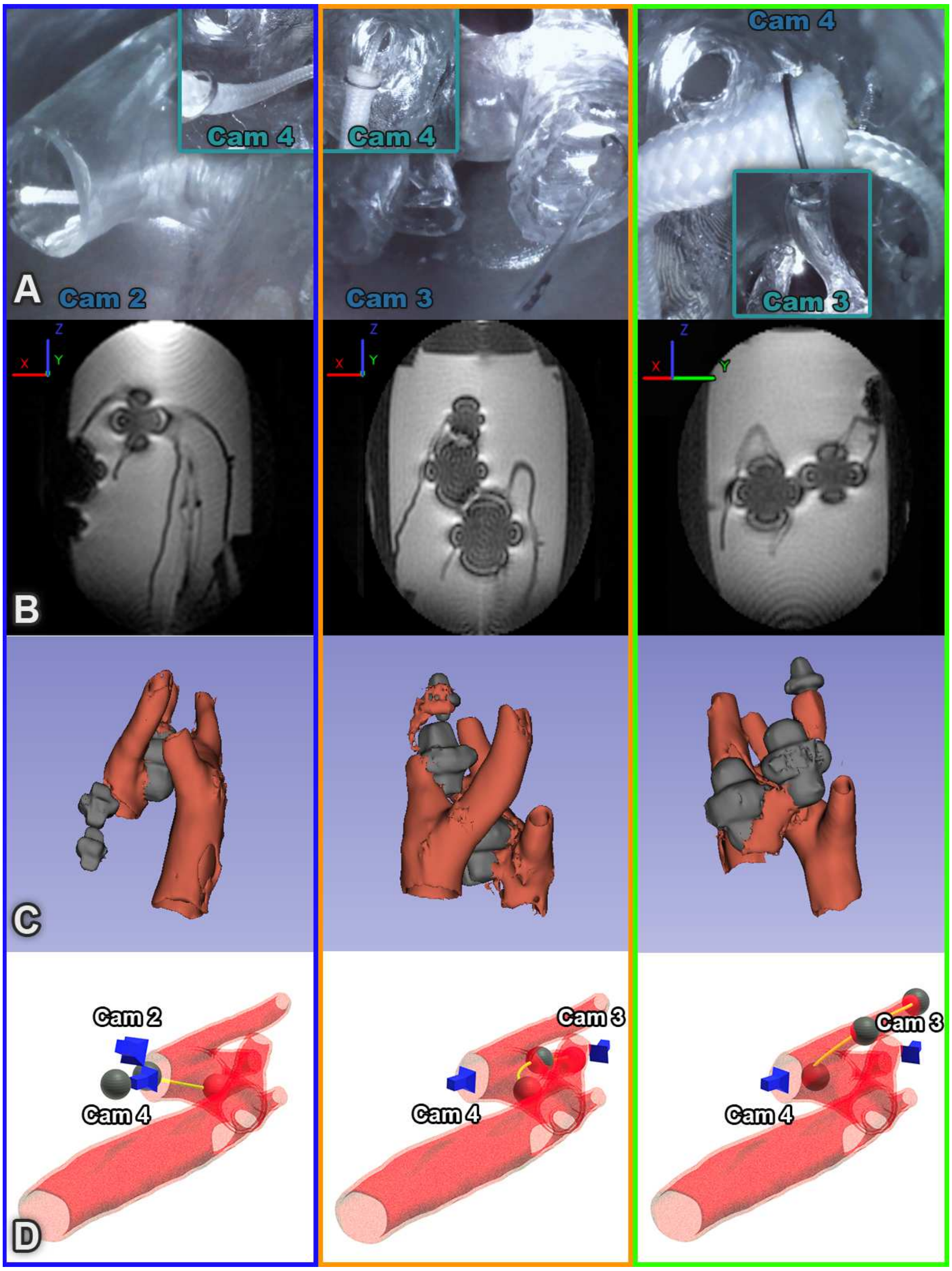

Figure 4: Visual and MR images of the aortic arch navigations (cont.). The left-hand column (blue surround) shows the ascending aorta (AA). The central column (orange surround) shows the right common carotid artery (RCA). Finally, the right-hand column (green surround) shows navigation into the right subclavian artery (RSA). (A) optical camera images, (B) 2D slice of the MR Image showing signal voids from ferrous components. Basis frame shown where B_0 always exists in the Z direction. (C) Reconstruction of anatomy and CoSMA shape based on 3D MRI data (3D Slicer), and (D) 3D rendering of phantom with reconstructed shape of the CoSMA and camera positions.

anisotropic material composition (braided nylon) allowing maximization of the twisting to bending stiffness ratio (GJ/EI - See Section 5.2). This enhanced ratio reduces the tendency of the device to exhibit the snap-through instability [5]. We have demonstrated a potential clinical use case with navigation into all the branches of the aortic arch

The geometry and referential orientation of the rings is critical to performance and we have shown how this design feature is encoded with our FE model and in our multi-sleeve numerical model (Section 5.5). The principle benefit of magnetic actuation lies in the potential for miniaturization and the only barrier to significant improvement on our 4 mm maximum diameter design lies in fabrication. MR image distortion has been experimentally minimized (Section 5.4) and clearly image distortion/signal voids would reduce further for a more miniaturized system. An earlier prototype of our catheter design leveraged thermoplastic elastomer (TPE) tubes from Arkema (https://www.arkema.com/global/en/) but the lack of torsional rigidity precluded the transmission of twist along the catheter length. This challenge can be mitigated using reinforced TPE (the only commercially available product we have thus far sourced uses non-MRI compatible, stainless steel, reinforcing).

Regarding image distortion, the plumes caused by the magnetic entities would vary in size as a function of $|B_0|$. A smaller background field (e.g. or 3T or even 1.5T clinical scanner) would reduce the signal void ([39]) without reducing magnetic torque, as long as magnetic saturation was still achieved (Equation 1). The orientation of this plume is always aligned with B_0 but the *shape* of the plume has been observed to vary as a function of the orientation of the ring. This makes navigation exclusively under MRI more challenging as tube orientation cannot be directly observed. There is a future work here on, either, analyzing the shape of the plume to determine the pose of the rings or, the addition of fiducial markers to extract CoSMA pose from the MR image. We have also observed the catheter to be agnostic to the imaging gradients with no measurable deformation observed during the imaging cycle.

Here we have presented a proof of concept for a new class of MRI-actuated and imaged concentric tube catheter. This article demonstrates a feasible solution to the significant challenge of developing a multi-DoF shape-forming, miniaturizable, self-sensing soft catheter. Future developments should focus on four major areas. (1) The rapid harvesting and post-processing of MRI information such that this potential wealth of sensory information can be usefully implemented by an operating model. (2) The operational hardware of the CoSMA (control of the position and orientation of the various sleeves) must be automated to allow actuation in response to feedback. (3) The current numerical model will need to be faster and more robust before it can offer a path to a closed-loop control solution. With these three key developments, the prospect of autonomous navigation will become realistic. Finally, (4) fabrication of the CoSMA should be both automated and miniaturized; the manufacturing and positioning of the magnetic elements currently represents a significant source of operational error. Finally, the only barrier to the CoSMA having an outer diameter of the order of 1 mm lies in sourcing MRI compatible reinforcing materials.

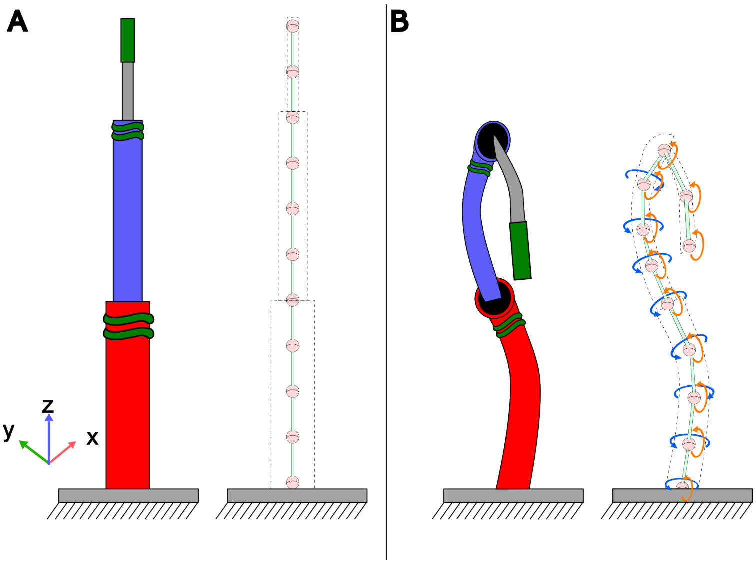

Figure 5: The 3D pseudo-rigid link model. (**A**) in referential pose and (**B**) in deformed pose. Magnetic torques are imparted at the locations of the magnetic elements (shown in green). These are balanced against elastic torques at each pseudo-joint. The full shape of the structure is encapsulated by the joint angle array ($\boldsymbol{Q}$) from which a Jacobian transpose ($\boldsymbol{J}^T$) can be constructed to map magnetic wrench ($\boldsymbol{S}$) to joint stiffness ($\boldsymbol{K}$). As detailed in Section 5.5, the three sleeves are independently modelled and then connected by interactive torques.

5 Methods

5.1 The Rigid Link Model

The system is modelled as a chain of pseudo-rigid links as described in detail in [40]. The rigid link model encapsulates bending and twisting behaviour but, in common with the Kirchhoff rod model, assumes shear stress and extension/compression to be zero. The continuum structure is discretized into n rigid links, each with a 3D joint, with the joint angle array given as:

$$\mathbf{Q} \in \mathbb{R}^{3n\times 1} = \begin{bmatrix}\mathbf{q}_0 & \cdots & \mathbf{q}_i & \cdots & \mathbf{q}_n\end{bmatrix}^T . \tag{2}$$

Where $\boldsymbol{q}_i$ represents the 3D joint angle at the i'th link. Joint stiffness is determined by the linear stiffness matrix (Section 5.2):

$$\mathbf{K} \in \mathbb{R}^{3n\times 3n} = \underbrace{diag(E_x I_x, E_y I_y, GJ)/L}_{\text{repeated diagonally } n \text{ times}} . \tag{3}$$

Where $E_x I_x$ and $E_y I_y$ comprise the elastic modulus and second moment of area and constitute bending stiffness about X and Y respectively and GJ comprise the shear modulus and the polar moment of area and constitute torsional stiffness about Z. L is the length of each joint. For extreme deformations (strain $> 100\%$), the assumptions of linear elasticity (Equation 3) break down but for the lower, linear strains we experience in this work, a relatively small number of links ($n \approx 16$) can be shown to be mesh independent.

The magnetic torque $\boldsymbol{\tau}_{mag}$ of each link is stacked into a wrench vector as:

$$\mathbf{S} \in \mathbb{R}^{6n\times 1} = \begin{bmatrix}0_{3\times 1} & \boldsymbol{\tau}_{mag_0} & \cdots & 0_{3\times 1} & \boldsymbol{\tau}_{mag_i} & \cdots & 0_{3\times 1} & \boldsymbol{\tau}_{mag_n}\end{bmatrix}^T \tag{4}$$

with the $0_{3\times 1}$ components representing the contribution of magnetic force, zero in our homogeneous background field. This torque is applied at the locations of the magnetic rings (or pin,

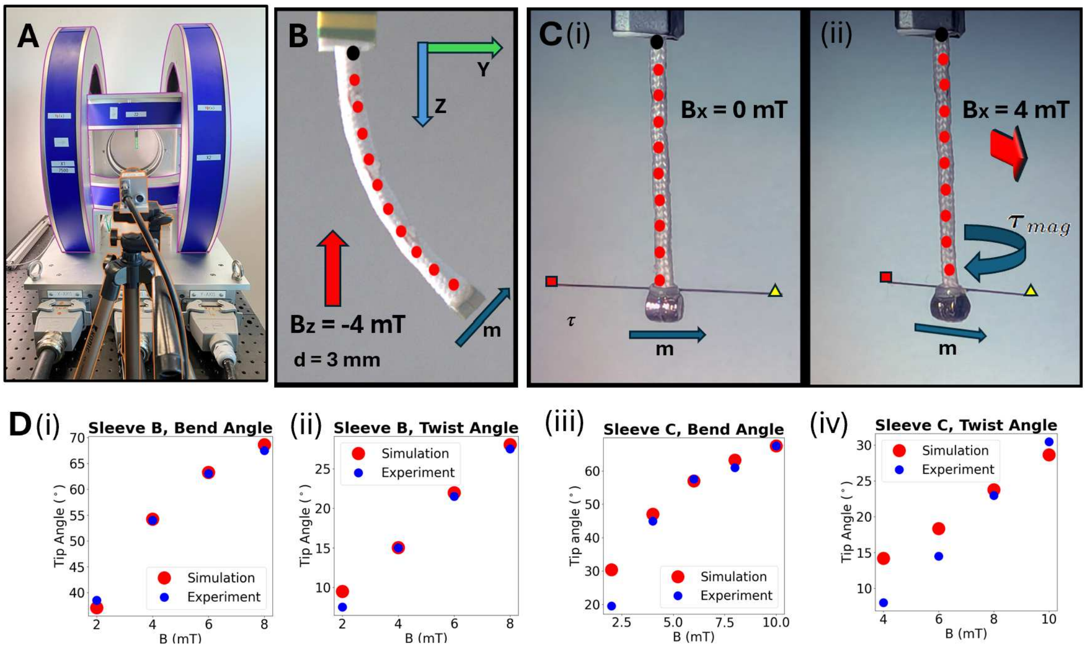

Figure 6: (A) The deformation experiment setup in the 3D Helmholtz coil (pink). The braid with magnet attached (green) is constrained with a 3D printed clip (blue) and the data gathered via a Basler camera (orange). (B) The 3 mm diameter braid (Sleeve C) subjected to a pure bending torque induced by a -4 mT field in our 3D Helmholtz coil with the results of the rigid link simulation projected in red. (C) The corresponding pure twisting torque on the same 3 mm diameter braid (Sleeve C). A Nitinol bar is attached to the magnet to extract pose data at (i) B = 0 and (ii) B = 4 mT in this example. (D) Graph of actuating field against tip angle for simulation (red) and experiment (blue). (i) The 1.5 mm diameter braid (sleeve B) under the bending primitive. (ii) The 1.5 mm diameter braid (sleeve B) under the twisting primitive. (iii) The 3 mm diameter braid (sleeve B) under the bending primitive. (iv) The 3 mm diameter braid (sleeve C) under the twisting primitive.

in the case of sleeve A) as described in Section 5.3 and set to zero for the magnetically inert sections of the CoSMA.

Finally, a complete expression balancing magnetic and elastic torques can be written as:

$$\mathbf{KQ} = \mathbf{J}^T\mathbf{S} \tag{5}$$

where $\mathbf{J}^T \in \mathbb{R}^{3n\times 6n}$ is the transpose of the differential kinematic Jacobian, itself a function of $\mathbf{Q}$ [40]. Consequently, no closed form solution exists and a convergent numerical solution must be applied as described in Section 5.5.

5.2 Mechanical Characterization

In order to determine the mechanical properties of the two braids, an experiment was devised employing remnant magnetic torque in a low field (< 10 mT) Helmholtz coil. Results are processed based on the modeling presented in Section 5.1. Any permanent magnet of magnetization $\boldsymbol{m}$ will experience an aligning torque in a background field ($\boldsymbol{\tau} = \boldsymbol{m} \times \boldsymbol{B}$) [26]. This known torque can thus be exploited to determine the elastic restoring forces within an anisotropic material such as our braid. By independently arranging the cross product about the Y and Z axis (see Fig. 5 for axes definitions) respectively, the stiffness of the braid can be determined under the isolated bending and twisting primitives. This information supplies the modelling assumptions in Section 5.5.

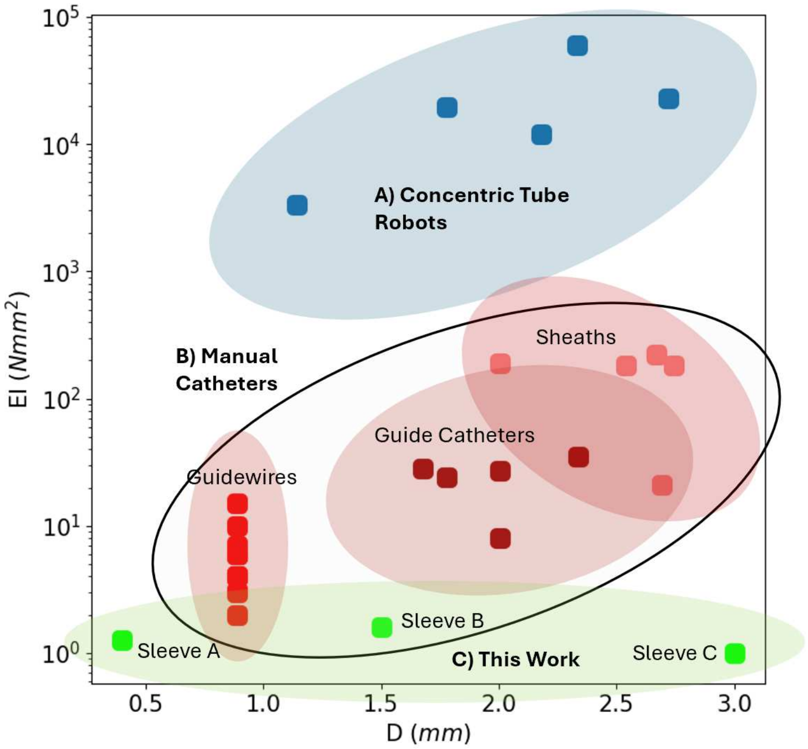

Figure 7: Comparison of Bending Stiffness (EI) against Diameter (D) for the state-of-the-art in: (A) Super-elastic concentric tube robots (in blue, taken from [8, 42]. (B) Clinical manual guidewires, catheters and sheaths (in red, taken from [34]). (C) This work (in green, taken from Section 5.2).

5.2.1 Bending Deformation

Each braid had a permanent magnet (4 mm length X 3 mm diameter, N52) attached to the distal end with magnetization aligned along the y-axis and was constrained at 20 mm and 30 mm lengths in the centre of our 3-D Helmholtz coil (3DXHC12.5-300, Dexing Magnet Tech. Co., Ltd, Xiamen, China) as shown in Fig. 6A. A homogeneous magnetic field was swept from -10 mT to +10 mT in the z-direction (-8 mT to +8 mT for sleeve B to avoid extreme deformation) and the results recorded via a Basler 25 mm zoom video camera (docs.baslerweb.com). Apple Keynote was used to gain the deformed tip angle from the still frames at each field. Given a remnant magnetization of 1.43 T, known magnet dimensions, magnet density of 7500 kg/m^3 for the gravity vector - added as a force to Equation 4, and known applied fields, Equation 5 can be solved to determine the bending stiffness (EI) of the braids. The bending stiffness of the 3 mm diameter braid (sleeve C) was calculated as $1.6 \times 10^{-6} \pm 2.1 \times 10^{-7} Nm^2$ and that of the 1.5 mm braid (sleeve B) as $1.0 \times 10^{-6} \pm 1.3 \times 10^{-7} Nm^2$. Sleeve A is manufactured from 0.4 mm diameter isotropic nylon (elastic modulus $E \approx 1\ GPa$, https://www.plastics.toray/technical) giving a calculated bending stiffness of EI $= 1.3 \times 10^{-6} Nm^2$. For the sake of comparison, a bending stiffness of $1.6 \times 10^{-6} Nm^2$ is equivalent to a Dragon Skin-10 catheter (elastic modulus $E \approx 200\ kPa$ [41]) of diameter 3.6 mm. Fig. 7 illustrates these bending stiffnesses in comparison with Nitinol concentric tube robots and clinical manual guidewires, catheters and sheaths.

5.2.2 Twisting Deformation

Using an identical setup as the deformation experiment with the exception of applied field orientation (See Fig. 6C), each braid was constrained again at 20 mm and 30 mm lengths. A magnetic field in the z-direction was applied to induce torque in the braid. Results were again analyzed using Apple Keynote and Equation 5 solved to determine the twisting stiffness (GJ) of the respective braids. In this arrangement the influence of gravity is zero. The twisting stiffness of the 3 mm diameter braid (sleeve C) was calculated as $1.9 \times 10^{-5} \pm 4.0 \times 10^{-6} Nm^2$ and that of the 1.5 mm braid (sleeve B) as $1.4 \times 10^{-5} \pm 2.1 \times 10^{-6} Nm^2$.

According to linear elasticity theory, for a slender rod of isotropic material, $\frac{GJ}{EI} = \frac{2}{3}$. For our 3 mm diameter braid (sleeve C) $\frac{GJ}{EI} = 12$. For our 1.5 mm diameter braid (sleeve B) $\frac{GJ}{EI} = 14$. This illustrates the $\approx 20X$ increase in ratio of twisting to bending stiffness afforded by the anisotropic behaviour of the braid, similar to that reported in [32]. This ratio $\frac{GJ}{EI}$ is fundamentally important to the snap-through instability exhibited in conventional concentric tube robots [5]. Using our proposed actuation strategy it becomes possible to exploit materials with both a much lower overall stiffness as well as a lower EI with respect to GJ. This is enabled as the magnetically induced torques (as compared to mechanically induced) significantly reduce transmission stiffness requirements.

5.3 Magnetic Characterization

Ferromagnetism is the property of a (not necessarily, but often, iron-based) material to display a strongly positive material susceptibility ($\chi \gg 0$) [43]. That is, to induce a parallel magnetic moment when subject to an applied field. Other forms of magnetically responsive material do exist (dia-, para-, ferri- and antiferro-magnetic), but, for the purposes of robotic actuation, display too weak a response to be considered here [43]. In order to determine the torque on a non-spherical ferromagnetic body in a background field we must first review the concept of demagnetization.

A ferromagnetic object exposed to a background field ($\mathbf{H_b}$) generates a demagnetizing field ($\mathbf{H_d}$) which acts to reduce the overall magnetic moment. The total field at any point is the sum of these two fields ($\mathbf{H} = \mathbf{H_b} + \mathbf{H_d}$) and the induced magnetization is related to the total field via the apparent susceptibility tensor, $\mathbf{M} = \boldsymbol{\chi_a}.\mathbf{H}$ [31] (Here the upper-case $\mathbf{M}$ denotes magnetization per unit volume in A/m, the same units as the field $\mathbf{H}$ thus $\boldsymbol{\chi_a}$ is dimensionless). The apparent susceptiblity tensor ($\boldsymbol{\chi_a} \in \mathbb{R}^{3\times3}$) can be shown, for sufficiently high material susceptibility ($\chi > 10^3$) to be inversely proportional to the demagnetization factors along the principle axes of the body $\boldsymbol{\chi_a} = diag(1/n_x, 1/n_y, 1/n_z)$ which, counter-intuitively, are purely a function of geometry [26]. In a strong background field, these demagnetization factors allow for exact determination of the magneto-static energy. Demagnetization factors are subject to the constraint $n_x + n_y + n_z = 1$ (for finite rings [44]) and, for radially symmetrical geometries, can be reduced to 1D as $n_y == n_z$. For the sake of convention, we rename the demagnetization factor in the axial direction as n_a and the two demagnetization factors in the radial directions as $n_r = (1 - n_a)/2$. Under ultra-high fields, such as our MRI system, saturation magnetization (m_s) will always be attained $|\mathbf{M}| \gg m_s$, thus, magnetic torque can be shown to be as given in Equation 1.

The demagnetizing fields of non-spherical geometries in a background field is an extensive area of physics research [44]. Here we touch on the subject with the express purpose of ascertaining the torque imparted on our magnetically active elements. According to Equation 1, if the demagnetization factors are known, then magnetic torque becomes a function of θ, the angle between the symmetrical axis of the magnetic element and the applied field. Consequently, this section is dedicated to determination of demagnetization factors (Section 5.3.1) and then a reconciliation of the magnetic torques on these shapes when placed in the MRI bore (Section 5.3.2).

5.3.1 Magneto-static Finite Element Model

The calculation of demagnetization factors relies on the assumption of uniform magnetization, implying a very strong applied field. This is not typically the case for robotic manipulation or actuation tasks [26], but is true in our case due to the large background field of the MRI system. For shapes

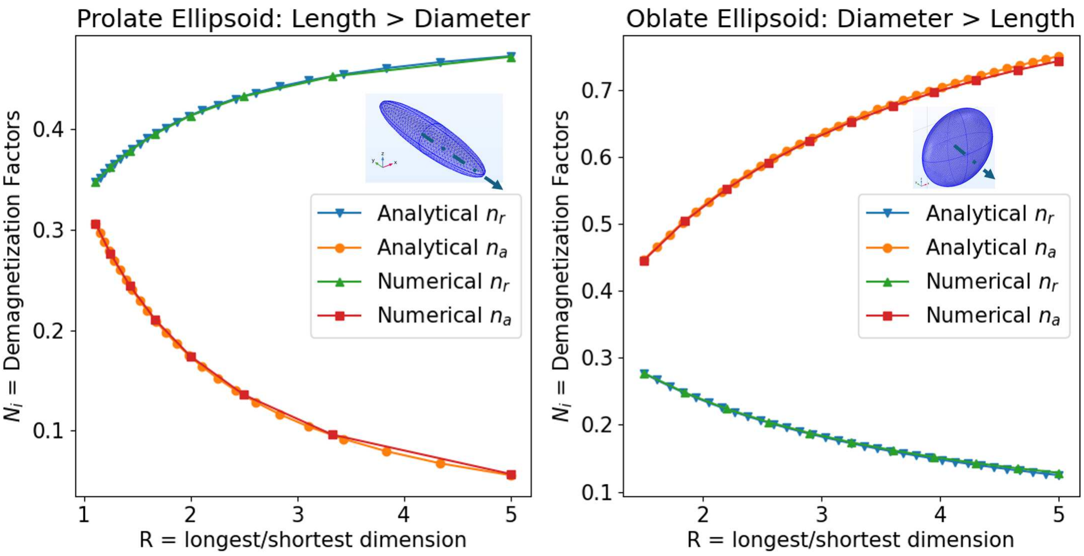

Figure 8: Comparison of demagnetization factors for prolate (left) and oblate (right) ellipsoids determined analytically from the formulae in [31] and via FEM according to the methodology detailed in Section 5.3.1. The RMS error here is below 1% in both scenarios confirming the validity of the FEM. This numerical approach can be thus generalized to complex geometries where comparative analytical solutions do not exist.

which can be approximated to ellipsoids of varying aspect ratio (i.e. a sphere or a rod) analytical solutions exist for these demagnetizing factors [26]. Analytical solutions have been addressed for more complex shapes such as hollow cylinders and shells [44, 45] but characterizing these geometries is cumbersome and such methods always require approximations. For the complex geometry presented here, that of a helical winding, the demagnetization factors must be determined experimentally or numerically (or both) [26].

For the numerical solution, a Finite Element Model (FEM) was constructed in the magnetostatics module of COMSOL multiphysics v6 (COMSOL AB, Stockholm, Sweden). Defining U as the scalar magnetic potential (in A) such that total field $\boldsymbol{H} = -\nabla U$ (in A/m). Because $\boldsymbol{H} = \boldsymbol{B}/\mu_0 - \boldsymbol{m}$ and $\nabla.\boldsymbol{B} == 0$ (where $\boldsymbol{B}$ is the magnetic flux density in T and $\boldsymbol{m}$ is the magnetic moment in A/m), $\nabla^2 U = \nabla \boldsymbol{m}$ within the material domain and $\nabla^2 U = 0$ outside the material domain (where $\boldsymbol{m} = 0$). Numerically solving these second order differential equations over a 500,000 node mesh generates a solution for the point-wise magnetization. This can be volumetrically integrated to determine the bulk magnetization vector ($\boldsymbol{M}$) which, given a known applied field, tells us the demagnetization factors from $\mathbf{M} = \boldsymbol{\chi_a H}$.

The numerical solution will solve for any geometry (as long as it can be robustly meshed) so, as an initial reconciliation of the FEM, we determine axial and radial demagnetization factors for the perfect ellipsoid presented analytically in [31] (Fig. 8). An RMS error below 1% confirms the accuracy of the numerical model described above. We then develop the model to represent the geometries of interest as shown in Fig. 9 generating the demagnetization factors shown in Table 1. These numbers are inputs to the reconciliation presented in Section 5.3.2.

5.3.2 Reconciliation of Magnetic Torques

Utilizing the rigid link simulation detailed in Section 5.2 in conjunction with magnetic properties from Section 5.3.1 we reconciled the deformation of single iron rings of both 4.0 mm diameter and 2.1 mm diameter over varying lengths ($L \in (5, 25)$ mm) in the bore of the MRI (Fig. 10). The experimental arrangement, harvesting and post-processing of optical images is consistent with

Table 1: Summary of demagnetization factors obtained via the FEM described in Section 5.3.1 for the geometry shown in Fig. 9A. The wire is annealed iron (99.5% purity, $m_s = 1.43 \times 10^6 A/m$) with a diameter of 0.25 mm. In the upper calculation, the loop has an outer diameter of 4.0 mm and in the lower calculation, an outer diameter of 2.1 mm (See Section 5.6). The magnetic torque (τ_{mag}) is calculated according to Equation 1 at peak ($\theta = 45°$).

	n_a	n_r	volume (mm^3)	$\tau_{mag}(mNm)$ at $\theta = 45°$
Ring Outer Diameter = 4.0 mm	0.95	0.03	0.62	0.73
Ring Outer Diameter = 2.1 mm	0.86	0.07	0.31	0.31

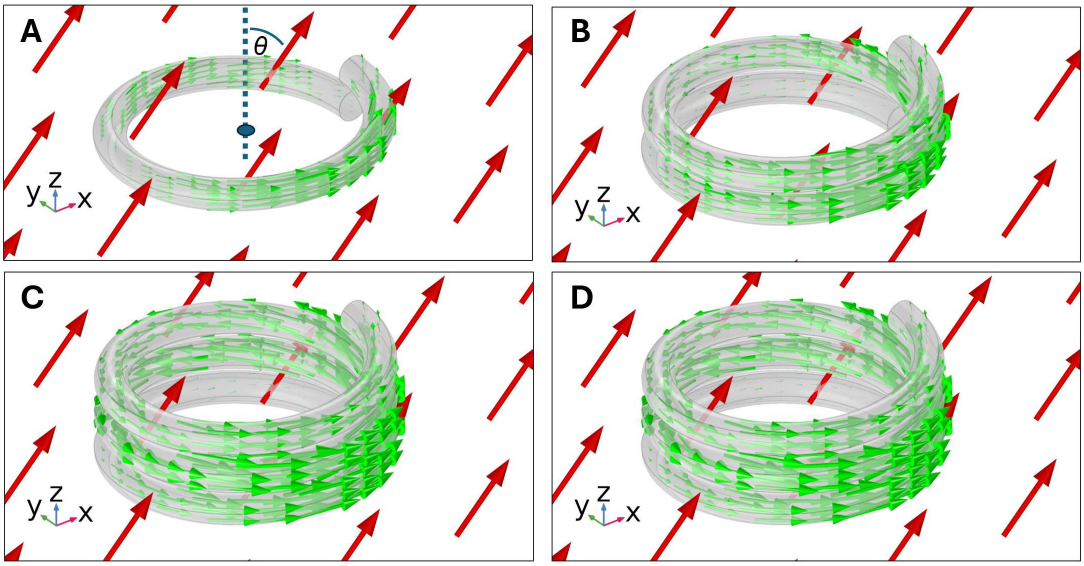

Figure 9: A 4.0mm diameter iron ring of (A) 1, (B) 2, (C) 3 and (D) 4 loops exposed to an arbitrary background field (red arrows). In this screenshot the field is applied equally in X and Z but for calculation of demagnetization factors, fields were swept about all axes. The demagnetizing field is solved over a 500,000 element mesh and the ratio of the volume integral of the induced magnetic moment (green arrows) to the applied field (red arrows) gives the susceptibility tensor ($\boldsymbol{\chi_a}$). This is a function purely of geometry and the results can thus be directly imported to the CoSMA simulation detailed in Section 5.5. (A) also shows the symmetrical axis of the ring and the angle (θ) between this axis and the applied field which drives Equation 1.

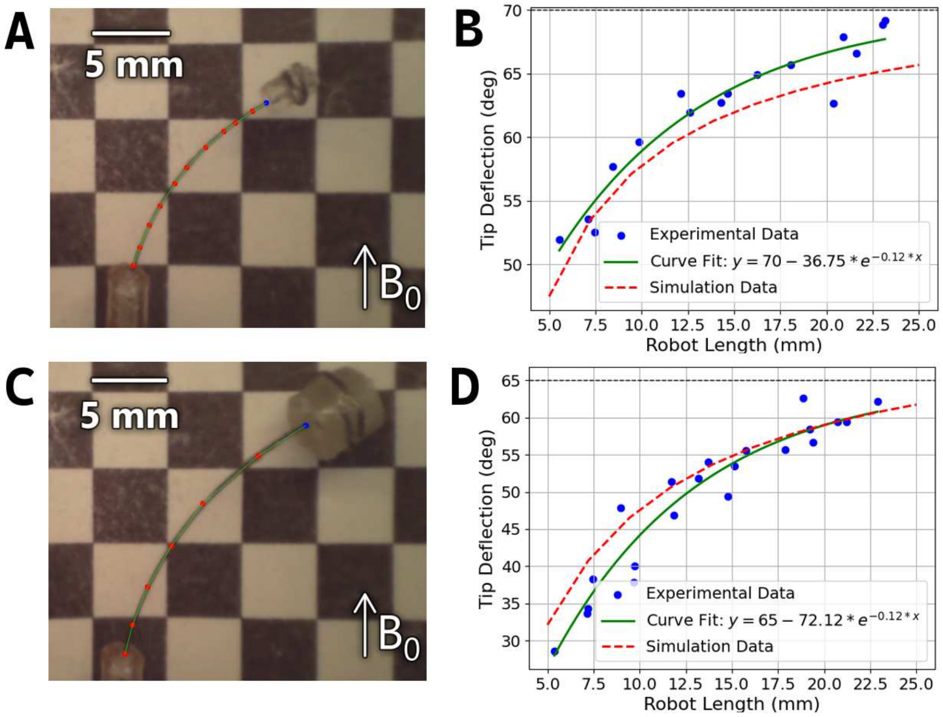

Figure 10: A single ring of iron wire near-orthogonally mounted at the tip of a length of Nitinol. The referential angle between B_0 and the symmetrical axis of the ring (θ_0) must be non-zero (to avoid model singularity) but arises mainly due to manual fabrication inaccuracy. θ_0 is measured for each specimen from the optical images and included as a variable in the rigid link model. (A) A 2.1 mm diameter ring was attached to 0.15 mm diameter Nitinol wire and placed in our 7T MRI bore. The unconstrained length of Nitinol was varied between 5 mm and 25 mm. (B) Three specimens were tested with $\overline{\theta_0} = 20°$. All experimental data-points appear as blue dots, the aggregated curve of these points - tip angle versus manipulator length (green curve) - appears against the corresponding deformations determined via the simulation (red curve) described in Section 5.1. Mean vertical projection percentage error across all data-points for the 2.1 mm diameter test was 4.5%. (C) The process is repeated for the 4.0 mm diameter ring on a 0.20 mm diameter Nitinol wire. (D) Three further specimens were tested with $\overline{\theta_0} = 25°$. Mean vertical projection percentage error across all data-points for the 4.0 mm diameter test was 2.9%.

Section 3.2. For the 4.0 mm diameter specimens, 0.2 mm diameter Nitinol was used as the deforming elastica, for the 2.1 mm diameter specimens, 0.15 mm diameter Nitinol was used. In all cases the Elastic modulus of Nitinol was assumed to be 70 GPa [46]. Each setting was repeated for three identically manufactured specimens. θ_0 - the referential angle between B_0 and the symmetrical axis of the ring was measured for each specimen from the optical images and included as a variable in the rigid link model. Vertical projection error was computed as the difference between the measured tip deflection from the real-world results and the corresponding deflection value predicted by the simulation data at the same manipulator length. From Fig. 10 the deformed tip angle, experimental versus simulation gives, for the 4.0 mm diameter experiment, RMS error of 2.0° (4.5% of mean tip angle) and for the 2.1 mm diameter experiment, RMS error of 1.8° (2.9% of mean tip angle).

5.3.3 Variation in Number of Windings

The rings affixed to the sleeves have, in our demonstrations, contained only one loop. This is to minimize the size of the signal void. It is possible to increase the number of loops on each ring (Fig. 9) which increases both torque (Table 2) and signal void size (Fig. 11). An increase in torque improves driveability of the CoSMA and allows for higher curvature bending.

5.4 MR System as Catheter Sensor

The volume of metal in the MRI bore, as well as image settings, have a significant impact on the information that can be gathered from the image. A further consideration here is the time taken to harvest and post-process the images. For any practical control application this speed consideration would need further refinement (e.g. as in [47]). To prove our concept on a preclinical MR system (Bruker BioSpin, Ettlingen, Germany), comprising of a horizontal 7T magnet, a gradient system with a maximum amplitude of 660mT/m, a quadrature-driven transmit-receive volume radiofrequency coil (inner diameter 72 mm), we employed a 3D ultra-short echo time (UTE) sequence with the following parameters: echo time TE = 0.011ms; repetition time TR = 20ms; 51360 projections; field of view $100 \times 60 \times 60$ mm, coronal orientation, reconstructed to $128 \times 128 \times 128$ points, image resolution: $781 \times 469 \times 469$ µm. Total acquisition time: 1027 seconds (≈17 minutes). Notably, the imaging time can be reduced by orders of magnitude by scanning a 2D plane determined by the output of any previous time step. A single 2D slice taken on the same settings generates an image in 8 seconds. Fig. 11 shows the artifacts in an example slice of the 3D UTE dataset, induced by 4 mm diameter rings of 1-4 loops (as in Section 5.3.3). These can be binary thresholded into either "signal" or "void" and thus characterized as total area of void and maximum length of void (Feret diameter) with results shown in Table 3. From this, and Fig. 11, it is clear (as expected) that reduced metal volume improves image fidelity although a diminishing return can be observed - each step reduction in metal volume affords less proportional improvement in image. This diminishing relationship is highlighted in the final column - void area per unit metal volume. The increased signal void could, in future works, be mitigated by (a) reducing the overall diameter of the CoSMA, (b) via targeted signal processing or (c) by exploiting machine learning methods [47] but these investigations are beyond the scope of this publication.

5.5 Simulation

Having characterized the mechanical properties of the continuous structures from which the CoSMA is constructed (Section 5.2) and the magnetic behaviour of our ferrous components (Section 5.3) we have sufficient data to populate a rigid link model (according to Section 5.1) of the complete system.

Table 2: Summary of demagnetization factors obtained via the FEM described in Section 5.3.1 for the geometry shown in Fig. 9. The wire is annealed iron (99.5% purity, $m_s = 1.43 \times 10^6 A/m$) with a diameter of 0.25 mm. In the upper calculation the loop has an outer diameter of 4.0 mm and in the lower calculation an outer diameter of 2.1 mm. The magnetic torque (τ_{mag}) is calculated according to equation 1 at peak ($\theta = 45°$). Note the diminishing returns in torque as loops are increased as axial demagnetization factor reduces.

Ring Outer Diameter = 4 mm				
number of loops (n)	n_a	n_r	volume (mm^3)	$\tau_{mag}(mNm)$ at $\theta = 45°$
1	0.95	0.03	0.62	0.73
2	0.90	0.05	1.23	1.34
3	0.85	0.08	1.85	1.84
4	0.81	0.10	2.47	2.26
Ring Outer Diameter = 2.1 mm				
number of loops (n)	n_a	n_r	volume (mm^3)	$\tau_{mag}(mNm)$ at $\theta = 45°$
1	0.86	0.07	0.31	0.31
2	0.73	0.14	0.62	0.47
3	0.63	0.18	0.93	0.53
4	0.56	0.22	1.23	0.54

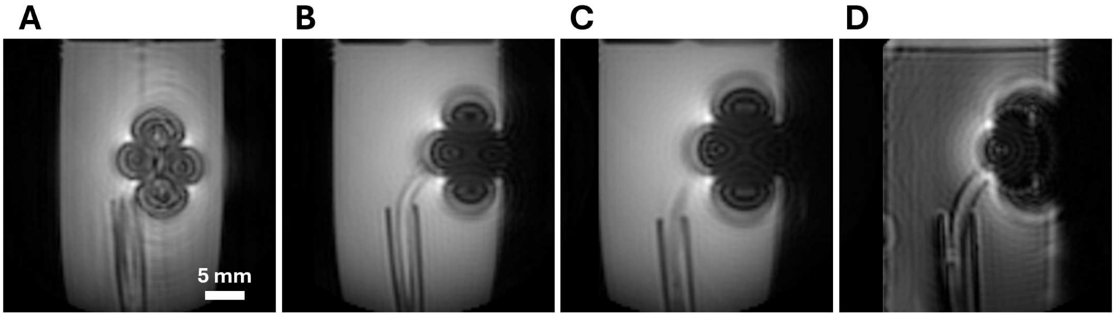

Figure 11: Signal voids generated by the presence of iron rings in MR images. A 20 mm length of 3.0 mm diameter braid was affixed with 4.0 mm diameter iron rings of 1, 2, 3 and 4 loops (corresponding to Figure 9 and Tables 2 and 3. Both the size and the intensity of image artifacts/signal voids are correlated with metal volume.

Table 3: Summary of metal volume, signal void area and signal void Feret diameter for the 4.0mm diameter rings (shown in Fig. 11). Void area per unit metal volume is also shown.

Number of loops (n)	Metal volume (mm^3)	Void area (mm^2)	Void Feret diameter (mm)	Void area per unit metal volume (mm^{-1})
1	0.6	370.6	27.2	601.4
2	1.2	433.6	30.0	351.8
3	1.8	519.3	32.9	280.5
4	2.5	694.6	34.1	281.7

Each sleeve was discretized into n pseudo rigid links with joint angles $\boldsymbol{Q} \in \mathbb{R}^{n\times 3}$. A point torque is applied at the tip determined according to Section 5.3 and the orientation of the magnetic element, itself a function of the joint angles, $\boldsymbol{\tau}_{mag}(\boldsymbol{Q}) \in \mathbb{R}^3$. Notably, τ_{mag} from equation 1 is planar (magnitude only) so, to convert this to $\mathbb{R}^3$, the torque direction must be ascertained. This is the unit vector of the cross product of the background field with the symmetrical axis of the magnetic element ($\boldsymbol{\tau}_{mag} = \tau_{mag}(\hat{\boldsymbol{B}} \times \hat{\boldsymbol{r}})$). Elastic torques ($\boldsymbol{\tau}_{ela}(\boldsymbol{Q}) \in \mathbb{R}^{n\times 3}$), determined from the stiffness matrices in Section 5.2 are balanced with magnetic torques according to $J\boldsymbol{\tau}_{mag} = K\boldsymbol{q}$ where J is the robot Jacobian as described in Section 5.1 of each of the respective sleeves. Hence, there are different J, K and $\boldsymbol{\tau}_{mag}$ values for each of the three sleeves. This torque balance propagates along each individual sleeve producing independent deformations ($\boldsymbol{Q_A}, \boldsymbol{Q_B}, \boldsymbol{Q_C}$).

The position, but not orientation, of each sleeve must be equal up to the distal point of each sequential sleeve. For instance, sleeve B is free to rotate but must be in the same location as sleeve C (as it is concentric) up until the end of sleeve C. Beyond this point sleeve B is unconstrained. To encode this constraint, an interactive force is applied equally and oppositely at each joint along the length of both concentric sleeves. This interactive force is computed according to the stiffness matrix and the vector difference in position at each location (e.g. $\boldsymbol{p}_{Bi} - \boldsymbol{p}_{Ci}$). This constrains (after some iterative loops) the concentric sleeves into the same position, despite having independent lengthwise orientation (q_z in the robot frame in Fig. 12) and therefore not necessarily having the same 3D joint angles. As a consequence of this modelling feature, the lengthwise orientation of each sleeve (*roll*) can be independently controlled as an input. This iterative numerical solution was solved (for $n = 24$ in the results presented), using an actively damped ($\mu(err) \in (2\%, 25\%)$ calculated as a function of current error) Newton–Raphson method converging in the range of 0.5-10 seconds.

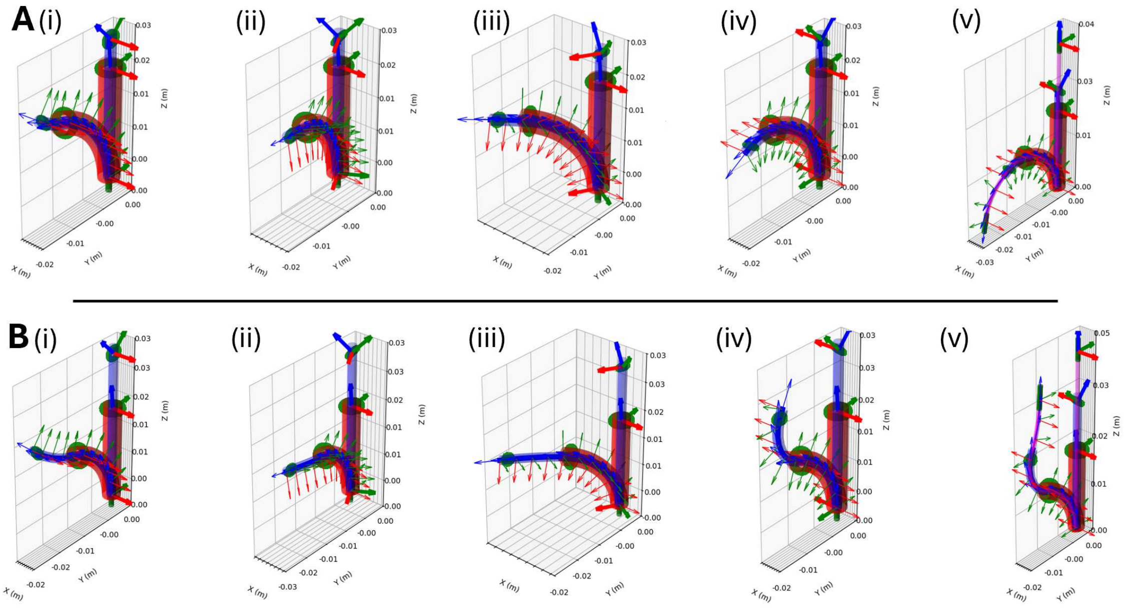

Figure 12: The output of our numerical simulation showing two step-wise progressions **(A)** and **(B)**. Referential pose is shown as 3D shapes, sleeve B in blue, sleeve C in red, referential ring positions in green with their basis frames (red-green-blue) in bold. Deformed pose is shown in the same colors with local basis frames along the continuum length. The homogeneous background field is in positive Z (vertically upwards here). **(A)** Sleeve B is 20 mm longer than sleeve C (initially sleeve A length = 0). (i) Rotation of sleeve B = 0°, this represents the default pose for this design. (ii, iii, iv) Sleeve B is rotated through 180° in 60° increments. Retroflexion is first observed when Sleeve B rotation exceeds 120°. (v) Sleeve A is inserted and, due to the retroflected Sleeve B, aligns negatively with B_0. **(B)** Sleeve B is 30 mm longer than sleeve C Again, sleeve B is rotated from 0° to 180° in 60° increments but the increased length of sleeve B induces a forward facing sigmoidal deformation. In (v) sleeve A is inserted and aligns positively with B_0. Although not demonstrated in this work, sleeve A could also have zero ferrous component which would result in tangential insertion beyond the tip of sleeve B.

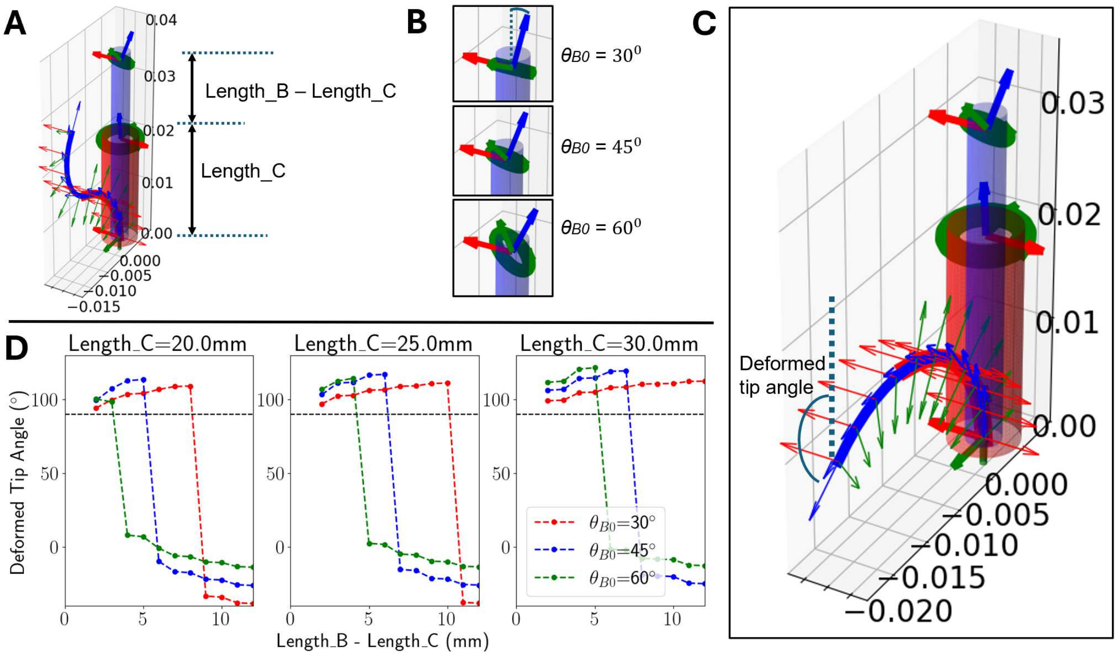

Figure 13: Curves showing the unconstrained length of sleeve B versus the deformed tip angle of sleeve B. Specifically, (A) illustrates the parameters for the length of sleeve C (Length_C) and the unconstrained length of sleeve B (Length_B - Length_C). In this particular sample the deformed configuration is sigmoidal (deformed tip angle $< 0°$). (B) Shows three different referential angles of the ring at the tip of sleeve B ($\theta_{B0} = 30°, 45°, 60°$) - this is the angle between the symmetrical axis of the ring and the applied field. (C) Shows the deformed tip angle parameter as well as a sample configuration where the deformed tip angle $> 90°$ - an example of the retroflected pose. (D) Plots the unconstrained length of sleeve B (X-axis) against deformed tip angles (Y-axis) for the three referential angles of ring B - the black checked line represents the criterion for retroflexion. As can be seen, smaller θ_{B0} (red curve) gives a larger stable region of retroflexion - i.e. retroflexion is possible for longer lengths of unconstrained sleeve B - but struggles to produce sigmoidal deformations (plot on the right). Conversely, larger θ_{B0} (green curve) readily produces the sigmoidal deformation but struggles to retroflect (plot on the left). For these settings, $\theta_{B0} = 45°$ gives a stable blend of retroflexion and sigmoidal deformations. A more exhaustive parameter optimization lies beyond the scope of this work, but this analysis justifies our design decision pertaining to θ_{B0}.

Branch	**Timestep**	**Sleeve A**	**Sleeve B**		**Sleeve C**		**RMS Error (mm)**
		Length (mm)	Length (mm)	Roll (°)	Length (mm)	Roll (°)	
Left Subclavian Artery (LSA)	1	5	10	0	5	-90	1.02
	2	5	15	0	5	-90	1.62
	3	5	25	0	10	-90	1.88
	4	35	25	0	10	-90	1.29
Left Common Carotid (LCA)	1	5	10	0	5	10	0.56
	2	5	20	0	10	10	0.95
	3	5	35	0	10	10	0.73
	4	45	35	0	10	10	1.55
Ascending Aorta (AA)	1	5	15	-85	10	55	1.30
	2	5	20	-85	10	60	1.02
	3	5	25	-85	15	60	0.92
	4	35	25	-85	15	60	1.18
Right Common Carotid (RCA)	1	5	15	0	10	45	1.43
	2	30	25	0	15	45	1.67
	3	5	30	175	20	245	0.88
	4	35	30	175	20	245	1.30
Right Subclavian Artery (RSA)	1	5	15	0	10	85	1.80
	2	5	20	0	10	-85	2.55
	3	5	35	0	20	-80	4.05
	4	40	35	0	20	-80	4.00

Table 4: Base configurations for the navigations shown in Figures 3 and 4 determined via the simulation described in Section 5.5. The five DoFs of the catheter are shown as length of sleeve A, length and roll of sleeve B and length and roll of sleeve C. Roll refers to rotation about the local Z-axis of the sleeve in question. Error (in mm) is calculated as the RMS of the spatial error between the lumen centre-line and the simulated position of each node of the 20 rigid links (as described in Section 5.1).

The principle design feature of the CoSMA is that of retroflexion. The referential orientation of ring C (θ_{C0}) is as close to 0° as possible (The symmetrical axis of the ring is aligned with the background field) meaning sleeve C deforms to an angle asymptotically approaching 90°. Sleeve B can then rotate and/or translate to achieve a wide variety of shapes, for some of which the tip of sleeve B is deformed beyond 90° (Fig. 12 and Fig. 2). This allows sleeve A to align either positively or negatively with the background field permitting the full 360° range of motion demonstrated in Fig. 2.

It is self evident that the torque magnitude of each sequential sleeve must be lower than the previous so as to not overpower the shape to which it is conforming, thus $|\boldsymbol{\tau_A}| < |\boldsymbol{\tau_B}| < |\boldsymbol{\tau_C}|$. Based on considerations in Section 5.4 regarding image distortion, the volume of metal throughout the CoSMA must be minimized to permit the clearest possible view of CoSMA shape and surrounding anatomy (Fig. 11). For this motive we used the minimum size of one loop for both ring B and ring C and the pin on sleeve A is 5 mm long. This arrangement is the smallest metal volume which provides sufficient torque to provide a full range of motion (for this particular set of sleeve materials and geometries). The constraint $\tau_B < \tau_C$ is met under this arrangement as the diameter of ring B is half that of ring C (see Table 1).

To ascertain a suitable angle to position ring B onto sleeve B we performed the numerical

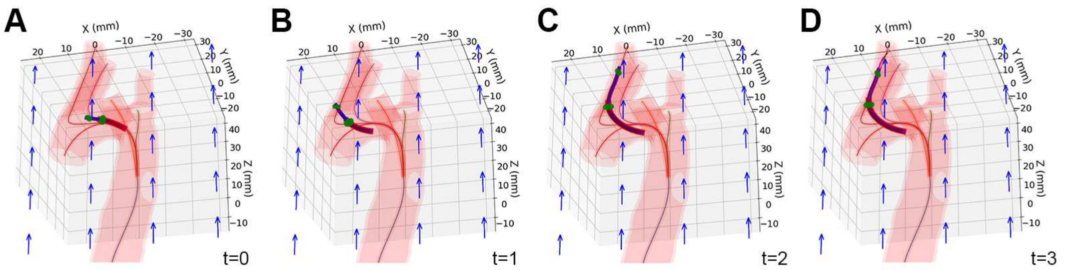

Figure 14: The four time-step simulated navigation into the right subclavian artery. The blue arrows indicate the unchanging background field B_0. Anatomical geometry outline is shown in transparent pink and centre-lines in red. The catheter follows the desired path according to the base configurations presented in Table 4. For this three-dimensional and sinuous navigation, spatial error from the geometric centre-line peaks at 4.05 mm - approximately equal to the mean radius of the anatomy through which it travels.

optimization shown in Fig. 13. The unconstrained length of sleeve B (defined as the length of sleeve B minus the length of sleeve C) is plotted against the deformed tip angle of sleeve B *after* the 180° rotation of sleeve B (Fig. 12A(iv) and B(iv)). Any deformed tip angle in excess of 90° represents retroflexion. For a longer unconstrained sleeve B, the CoSMA will deform into the sigmoidal shape as sleeve B rotates (Fig. 12B(iv)). This shape is represented in Fig. 13D as the right hand region of negative tip angles. The angle at which ring B is mounted (represented by the different curves) determines the length of sleeve B which can stably support retroflexion before the CoSMA flips into the sigmoidal deformation mode. It can be observed that smaller θ_{B0} (red curve) gives a larger stable region of retroflexion - i.e. retroflexion is possible for longer lengths of unconstrained sleeve B - but struggles to produce sigmoidal deformations. Conversely, larger θ_{B0} (green curve) readily produces the sigmoidal deformation but struggles to retroflect. For these settings, $\theta_{B0} = 45°$ gives a stable blend of retroflexion and sigmoidal deformations.

5.5.1 Simulated Aortic Arch Navigation

We leveraged the rigid link model described in Section 5.5 to ascertain the requisite base configurations for navigation into each of the five branches of the aortic arch phantom (Section 3.2). Path centre-lines were extracted in 3D Slicer 5.8.1 (https://www.slicer.org/) and loaded into our custom interactive simulation environment, where direct operator control could explore this synthetic search-space. Using this environment, the base configurations to navigate each pathway in a minimal contact manner were predetermined. A more robust path-planning process is clearly a prerequisite for any control application, a task which lies beyond the scope of this work. Each of the five navigations was discretized into four equal time-steps. Base configurations and RMS error values for the four time-steps and five paths are shown in Table 4, and the results of these simulated navigations are shown in the Supplementary Video S3. Additionally, Fig. 14 shows our four time-step simulated navigation into the most sinuous of the five target arteries - the Right Subclavian Artery (RSA). As can be seen in Table 4, the spatial error is generally of the order of 1 mm and, with the exception of the RSA, below 2 mm. For the RSA navigation spatial error peaks at 4.05 mm. Considering a mean radius of the RSA of 4 mm [48] we would expect this level of error to incur some small amount of anatomical contact which is reflected in the Supplementary Video S3. For the other four navigations, with the errors presented, no anatomical contact would be expected.

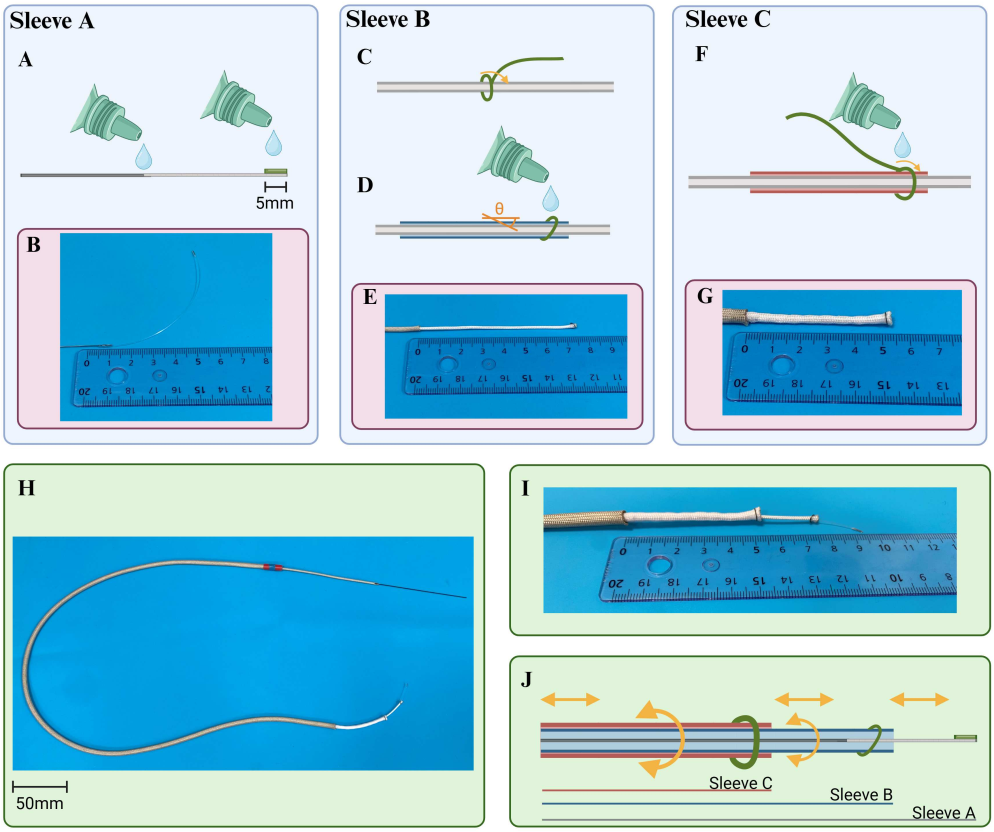

Figure 15: Fabrication Process of the CoSMA: (A,B) Sleeve A, a 5 mm iron pin is superglued to 0.4 mm diameter nylon wire. (C) Sleeve B, iron wire is wound orthogonally around a 2.1 mm diameter temporary rod. (D,E) This winding is superglued at a 45° angle onto the 1.5 mm diameter 75 mm length braid. (F,G) Sleeve C, iron wire is orthogonally wound around the 3 mm diameter, 50 mm length braid and secured with superglue. (H-J) The full shape forming catheter exhibits 5 DoFs (yellow arrows). Sleeves B and C are connected to 600 mm concentric fibreglass sleeves to enable mechanical control from outside the MRI system.

5.6 Fabrication

With reference to Fig. 15 and Supplementary Video S4, to create sleeve A, 5 mm of 0.25 mm diameter iron wire (GF44272571 Iron Wire Reel - Merck KGaA, Darmstadt, Germany) was superglued (Everbuild HV50 Industrial Superglue - Silka Limited, Welwyn Garden City, UK) in axial alignment to a 100 mm length of 0.4 mm diameter nylon wire (Vantage Pro 1/4 Pound Transparent - Fladen Fishing AB, Varberg, Sweden). This was attached with the same superglue to an 800 mm long, 0.15 mm diameter nitinol rod (Super-Elastic Nitinol Wire - McMaster-Carr, Elmhurst, USA). For Sleeve B, the same 0.25 mm diameter iron wire was wound once orthogonally onto a 2.1 mm diameter temporary rod. The diameter of the temporary rod was determined from the 45° angle at which the iron ring must sit on the 1.5 mm diameter braided sleeve ($\sqrt{1.5^2 + 1.5^2} = 2.1$). The rod ensures the windings will be circular (as opposed to elliptical) and thus exhibit no alignment bias when exposed to the background field. This ring was superglued to a 1.5 mm diameter, 75 mm length, nylon braid (Everlasto - James Lever 1856 Ltd, Manchester, UK). For Sleeve C, a 50 mm long, 3 mm diameter braided nylon sleeve (Lead-Weight Tape 100 g - Merrick & Day, Lincolnshire, UK) was threaded onto a temporary rod of 2.5 mm diameter. The same iron wire was wound once orthogonally around this sleeve and secured with superglue.

The base of sleeves B and C of the CoSMA was attached to ~ 600 mm of concentric fibreglass cable sleeve (Hellermann-Tyton international, www.HellermannTyton.com), via heat fusion, to allow manual mechanical control from outside of the bore of the MRI system. Finally, Sleeve A was inserted into Sleeve B and both into Sleeve C to form the full shape forming catheter shown in Fig. 15(h,i). 5 DoFs can be achieved due to independent translation of all 3 sleeves, and rotation around the central axis of Sleeves B and C (Sleeve A is axially symmetric).

References

[1] Rus, Daniela and Tolley, Michael T. “Design, fabrication and control of soft robots”. In: *Nature* 521.7553 (2015), pp. 467–475.

[2] Veiga, Tomas da, Chandler, James H, Lloyd, Peter, Pittiglio, Giovanni, Wilkinson, Nathan J, Hoshiar, Ali K, Harris, Russell A, and Valdastri, Pietro. “Challenges of continuum robots in clinical context: a review”. In: *Progress in Biomedical Engineering* 2.3 (2020), p. 032003.

[3] Wang, Zihan, Klingner, Anke, Magdanz, Veronika, Misra, Sarthak, and Khalil, Islam SM. “Soft Bio-Microrobots: Toward Biomedical Applications”. In: *Advanced Intelligent Systems* 6.2 (2024), p. 2300093.

[4] Kim, Yoonho, Parada, German A, Liu, Shengduo, and Zhao, Xuanhe. “Ferromagnetic soft continuum robots”. In: *Science robotics* 4.33 (2019), eaax7329.

[5] Gilbert, Hunter B, Rucker, D Caleb, and Webster III, Robert J. “Concentric tube robots: The state of the art and future directions”. In: *Robotics Research: The 16th International Symposium ISRR*. Springer. 2016, pp. 253–269.

[6] Su, Hao, Cardona, Diana C, Shang, Weijian, Camilo, Alexander, Cole, Gregory A, Rucker, D Caleb, Webster, Robert J, and Fischer, Gregory S. “A MRI-guided concentric tube continuum robot with piezoelectric actuation: A feasibility study”. In: *2012 IEEE International Conference on Robotics and Automation*. IEEE. 2012, pp. 1939–1945.

[7] Rucker, D Caleb, Webster III, Robert J, Chirikjian, Gregory S, and Cowan, Noah J. “Equilibrium conformations of concentric-tube continuum robots”. In: *The International journal of robotics research* 29.10 (2010), pp. 1263–1280.

[8] Rucker, Daniel Caleb and Gilbert, Hunter Bryant. *Methods for improving stability of concentric tube steerable devices using asymmetric flexural rigidity.* US Patent 11,964,387. Apr. 2024.

[9] Peyron, Quentin, Boehler, Quentin, Rougeot, Patrick, Roux, Pierre, Nelson, Bradley J, Andreff, Nicolas, Rabenorosoa, Kanty, and Renaud, Pierre. "Magnetic concentric tube robots: Introduction and analysis". In: *The International Journal of Robotics Research* 41.4 (2022), pp. 418–440.

[10] Li, Zhengyang and Xu, Qingsong. "Multi-Section magnetic soft robot with multirobot navigation system for vasculature intervention". In: *Cyborg and Bionic Systems* 5 (2024), p. 0188.

[11] Liu, Huibin, Teng, Xiangyu, Qiao, Zezheng, Yu, Haibo, Cai, Shuxiang, and Yang, Wenguang. "A concentric tube magnetic continuum robot with multiple stiffness levels and high flexibility for potential endovascular intervention". In: *Journal of Magnetism and Magnetic Materials* 597 (2024), p. 172023.

[12] Pane, S, Zhang, M, Iacovacci, V, Zhang, L, and Menciassi, A. "Contrast-enhanced ultrasound tracking of helical propellers with acoustic phase analysis and comparison with color Doppler". In: *APL bioengineering* 6.3 (2022).

[13] Thomas, Theodosia Lourdes, Sikorski, Jakub, Ananthasuresh, GK, Venkiteswaran, Venkatasubramanian Kalpathy, and Misra, Sarthak. "Design, sensing, and control of a magnetic compliant continuum manipulator". In: *IEEE Transactions on Medical Robotics and Bionics* 4.4 (2022), pp. 910–921.

[14] Fischer, Felix, Gletter, Christian, Jeong, Moonkwang, and Qiu, Tian. "Magneto-oscillatory localization for small-scale robots". In: *npj Robotics* 2.1 (2024), p. 1.

[15] Kilbride, Bridget F, Narsinh, Kazim H, Jordan, Caroline D, Mueller, Kerstin, Moore, Teri, Martin, Alastair J, Wilson, Mark W, and Hetts, Steven W. "MRI-guided endovascular intervention: current methods and future potential". In: *Expert review of medical devices* 19.10 (2022), pp. 763–778.

[16] Erin, Onder, Boyvat, Mustafa, Tiryaki, Mehmet Efe, Phelan, Martin, and Sitti, Metin. "Magnetic resonance imaging system–driven medical robotics". In: *Advanced Intelligent Systems* 2.2 (2020), p. 1900110.

[17] Zhang, Ke, Krafft, Axel Joachim, Umathum, Reiner, Maier, Florian, Semmler, Wolfhard, and Bock, Michael. "Real-time MR navigation and localization of an intravascular catheter with ferromagnetic components". In: *Magnetic Resonance Materials in Physics, Biology and Medicine* 23 (2010), pp. 153–163.

[18] Gosselin, Frédérick P, Lalande, Viviane, and Martel, Sylvain. "Characterization of the deflections of a catheter steered using a magnetic resonance imaging system". In: *Medical physics* 38.9 (2011), pp. 4994–5002.

[19] Tiryaki, Mehmet Efe, Doğangün, Fatih, Dayan, Cem Balda, Wrede, Paul, and Sitti, Metin. "MRI-powered Magnetic Miniature Capsule Robot with HIFU-controlled On-demand Drug Delivery". In: *2023 IEEE International Conference on Robotics and Automation (ICRA).* IEEE. 2023, pp. 5420–5425.

[20] Bergeles, Christos, Vartholomeos, Panagiotis, Qin, Lei, and Dupont, Pierre E. "Closed-loop commutation control of an MRI-powered robot actuator". In: *2013 IEEE international conference on robotics and automation.* IEEE. 2013, pp. 698–703.

[21] Murasovs, Nikita, Lloyd, Peter, Bacchetti, Alistair, May, Yael L, Armitage, Joshua, Cespedes, Oscar, Dall'Armellina, Erica, Chandler, James H, Schneider, Jürgen E, and Valdastri, Pietro. "Gradient pulling of a tethered robot via a magnetic resonance imaging system". In: *Device* (2025).

[22] Azizi, Arash, Tremblay, Charles C, Gagné, Kévin, and Martel, Sylvain. “Using the fringe field of a clinical MRI scanner enables robotic navigation of tethered instruments in deeper vascular regions”. In: *Science Robotics* 4.36 (2019), eaax7342.

[23] Tuna, E Erdem, Liu, Taoming, Jackson, Russell C, Poirot, Nate Lombard, Russell, Mac, and Çavuşoğlu, M Cenk. “Analysis of dynamic response of an MRI-guided magnetically-actuated steerable catheter system”. In: *2018 IEEE/RSJ International Conference on Intelligent Robots and Systems (IROS)*. IEEE. 2018, pp. 1–9.

[24] Phelan III, Martin F. “Interventional Lorentz Force-Based Actuation under Magnetic Resonance Imaging”. PhD thesis. Carnegie Mellon University, 2022.

[25] Pittiglio, Giovanni, Chandler, James H, Veiga, Tomas da, Koszowska, Zaneta, Brockdorff, Michael, Lloyd, Peter, Barry, Katie L, Harris, Russell A, McLaughlan, James, Pompili, Cecilia, et al. “Personalized magnetic tentacles for targeted photothermal cancer therapy in peripheral lungs”. In: *Communications Engineering* 2.1 (2023), p. 50.

[26] Abbott, Jake J, Diller, Eric, and Petruska, Andrew J. “Magnetic methods in robotics”. In: *Annual Review of Control, Robotics, and Autonomous Systems* 3.1 (2020), pp. 57–90.

[27] Schmauch, Marissa M, Mishra, Sumeet R, Evans, Emily E, Velev, Orlin D, and Tracy, Joseph B. “Chained iron microparticles for directionally controlled actuation of soft robots”. In: *ACS applied materials & interfaces* 9.13 (2017), pp. 11895–11901.

[28] Mishra, Sumeet R, Dickey, Michael D, Velev, Orlin D, and Tracy, Joseph B. “Selective and directional actuation of elastomer films using chained magnetic nanoparticles”. In: *Nanoscale* 8.3 (2016), pp. 1309–1313.

[29] Webster, Robert J, Romano, Joseph M, and Cowan, Noah J. “Mechanics of precurved-tube continuum robots”. In: *IEEE transactions on robotics* 25.1 (2008), pp. 67–78.

[30] Bergeles, Christos, Gosline, Andrew H, Vasilyev, Nikolay V, Codd, Patrick J, Del Nido, Pedro J, and Dupont, Pierre E. “Concentric tube robot design and optimization based on task and anatomical constraints”. In: *IEEE Transactions on Robotics* 31.1 (2015), pp. 67–84.

[31] Abbott, Jake J, Ergeneman, Olgaç, Kummer, Michael P, Hirt, Ann M, and Nelson, Bradley J. “Modeling magnetic torque and force for controlled manipulation of soft-magnetic bodies”. In: *IEEE Transactions on Robotics* 23.6 (2007), pp. 1247–1252.

[32] Lloyd, Peter, Onaizah, Onaizah, Pittiglio, Giovanni, Vithanage, Damith Katudampe, Chandler, James H, and Valdastri, Pietro. “Magnetic soft continuum robots with braided reinforcement”. In: *IEEE Robotics and Automation Letters* 7.4 (2022), pp. 9770–9777.

[33] Bozorth, Richard M. “Technical and Pure Iron”. In: *Ferromagnetism*. 1978, pp. 48–66. DOI: 10.1109/9780470544624.ch3.

[34] Qiu, Michael Y., Suskin, Charles B, Becerra-Garcia, Juan J., Roberts, Sophia H., Rucker, DeVaughn G., Zayed, Mohamed A., Osbun, Joshua W., and Genin, Guy M. *Quantification of the flexural rigidity of endovascular surgical devices using three-point bending tests*. 2023.

[35] Manda, Yugandhar R. and Baradhi, Krishna M. *Cardiac Catheterization Risks and Complications*. StatPearls Publishing, Treasure Island (FL), 2025.

[36] Sadler, Matthew and Lawson, Clive. “Cardiac catheterisation: avoiding common pitfalls with transradial vascular access”. In: *The British Journal of Cardiology* 30.3 (2023), p. 21.

[37] Beyar, Rafael, Davies, Justin, Cook, Christopher, Dudek, Dariusz, Cummins, Paul, and Bruining, Nico. “Robotics, imaging, and artificial intelligence in the catheterisation laboratory: Cath lab robotics, imaging, and AI”. In: *EuroIntervention* 17.7 (2021), p. 537.

[38] Wegermann, Zachary K, Swaminathan, Rajesh V, and Rao, Sunil V. “Cath lab robotics: paradigm change in interventional cardiology?” In: *Current Cardiology Reports* 21.10 (2019), p. 119.

[39] Jungmann, Pia M, Agten, Christoph A, Pfirrmann, Christian W, and Sutter, Reto. “Advances in MRI around metal”. In: *Journal of Magnetic Resonance Imaging* 46.4 (2017), pp. 972–991.

[40] Lloyd, Peter, Pittiglio, Giovanni, Chandler, James H, and Valdastri, Pietro. “Optimal design of soft continuum magnetic robots under follow-the-leader shape forming actuation”. In: *2020 International Symposium on Medical Robotics (ISMR)*. IEEE. 2020, pp. 111–117.

[41] Da Veiga, Tomás, Chandler, James H, Pittiglio, Giovanni, Lloyd, Peter, Holdar, Mohammad, Onaizah, Onaizah, Alazmani, Ali, and Valdastri, Pietro. “Material characterization for magnetic soft robots”. In: *2021 IEEE 4th International Conference on Soft Robotics (RoboSoft)*. IEEE. 2021, pp. 335–342.

[42] Modes, Vincent and Burgner-Kahrs, Jessica. “Calibration of Concentric Tube Continuum Robots: Automatic Alignment of Precurved Elastic Tubes”. In: *IEEE Robotics and Automation Letters* 5.1 (2020), pp. 103–110. DOI: 10.1109/LRA.2019.2946060.

[43] Kim, Yoonho and Zhao, Xuanhe. “Magnetic soft materials and robots”. In: *Chemical reviews* 122.5 (2022), pp. 5317–5364.

[44] Beleggia, Marco, Vokoun, D, and De Graef, M. “Demagnetization factors for cylindrical shells and related shapes”. In: *Journal of Magnetism and Magnetic Materials* 321.9 (2009), pp. 1306–1315.

[45] Parq, Jae-Hyeon. “Magnetometric demagnetization factors for hollow cylinders”. In: *Journal of Magnetics* 22.4 (2017), pp. 550–556.

[46] Lee, Pei-Yuan, Chen, Yen-Nien, Hu, Jin-Jia, and Chang, Chih-Han. “Comparison of mechanical stability of elastic titanium, nickel-titanium, and stainless steel nails used in the fixation of diaphyseal long bone fractures”. In: *Materials* 11.11 (2018), p. 2159.

[47] Tiryaki, Mehmet Efe and Sitti, Metin. “Magnetic Resonance Imaging-Based Tracking and Navigation of Submillimeter-Scale Wireless Magnetic Robots”. In: *Advanced Intelligent Systems* 4.4 (2022), p. 2100178.

[48] Anantha-Narayanan, Mahesh and Nagpal, MD. “Carotid, Vertebral, and Brachiocephalic”. In: *Updates in Peripheral Vascular Intervention, An Issue of Interventional Cardiology Clinics* 9.2 (2020), p. 139.

Acknowledgements

This work was supported in part by the Engineering and Physical Sciences Research Council (EPSRC) under Grants EP/Y037235/1 and EP/V009818/1, the European Research Council (ERC) through the European Union’s Horizon 2020 Research and Innovation Programme under Grant 818045, and by the National Institute for Health and Care Research (NIHR) Leeds Biomedical Research Centre (BRC) (NIHR203331). Additionally, JES acknowledges funding from the Wellcome Trust (219420/Z/19/Z) and the MRC (MR/X502789/1). Any opinions, findings, and conclusions, or recommendations expressed in this article are those of the authors and do not necessarily reflect the views of the EPSRC, the ERC, the NIHR, the Wellcome Trust, or the MRC. We also thank Leah Khazin, Ampere Kui and Samwise Wilson for technical support throughout. P.L., N.M., Y.L.M., A.B, V.F., B.C., J.D, J.E.S. and P.V. are with the STORM lab, department of Electrical and Electronic Engineering, University of Leeds, United Kingdom. E.D.A. and J.E.S are with the ePIC lab, Leeds Institute of Cardiovascular and Metabolic Medicine, University of Leeds, United Kingdom.

Peter Lloyd and Nikita Murasovs contributed equally to this work and should be considered joint first authors.

Author contributions

P.L. and N.M. conceived, designed and executed the study. J.E.S performed MRI acquisition. Y.L.M., A.B and V.F. contributed to data aggregation and analysis. B.C. and J.D contributed to results analysis. P.L., J.E.S. and P.V. supervised the project. P.L. and N.M. wrote the manuscript. J.H.C., E.D.A., J.E.S. and P.V. revised and reviewed the manuscript. All authors discussed the results and commented on the manuscript.

Competing interests

The authors declare no competing interests.

Additional information

Correspondence and requests for materials should be addressed to Peter Lloyd (p.lloyd@leeds.ac.uk) or Pietro Valdastri (p.valdastri@leeds.ac.uk).

Data availability

Any additional information required to reanalyze the data reported in this paper is available from the lead contact upon request.

Code availability

Any code utilized in this paper is available from the lead contact upon request.

Supplementary Files

This is a list of supplementary files associated with this preprint. Click to download.

- S1OverviewandPrincipleofOperation.mp4
- S2Freespacedemonstration.mp4
- S3AorticArchNavigations.mp4
- S4Manufacturing.mp4